frontiers in Earth Science

ORIGINAL RESEARCH
published: 28 July 2020
doi: 10.3389/feart.2020.00311

# Late Jurassic Leucogranites of Macau (SE China): A Record of Crustal Recycling During the Early Yanshanian Orogeny

*J. Gregory Shellnutt[1]*, Matthew W. Vaughan[2], Hao-Yang Lee[3] and Yoshiyuki Iizuka[3]*

*[1] Department of Earth Sciences, National Taiwan Normal University, Taipei, Taiwan, [2] Siletzia Resources, Lake Oswego, OR, United States, [3] Institute of Earth Sciences, Academia Sinica, Taipei, Taiwan*

OPEN ACCESS

**Edited by:**
*Patrizia Fiannacca, University of Catania, Italy*

**Reviewed by:**
*Mei-Fu Zhou, The University of Hong Kong, Hong Kong*
*Veronique Gardien, Université Claude Bernard Lyon 1, France*
*Federico Farina, Université de Genève, Switzerland*

***Correspondence:**
*J. Gregory Shellnutt*
*jgshelln@ntnu.edu.tw*

**Specialty section:**
*This article was submitted to Petrology, a section of the journal Frontiers in Earth Science*

**Received:** *09 March 2020*
**Accepted:** *30 June 2020*
**Published:** *28 July 2020*

**Citation:**
*Shellnutt JG, Vaughan MW, Lee H-Y and Iizuka Y (2020) Late Jurassic Leucogranites of Macau (SE China): A Record of Crustal Recycling During the Early Yanshanian Orogeny. Front. Earth Sci. 8:311. doi: 10.3389/feart.2020.00311*

The Yanshanian Orogeny consists of Jurassic to Cretaceous compressional-extensional cycles related to the subduction of the Paleo-Pacific Ocean beneath East Asia. Numerous granitic plutons were emplaced across southeast China at distinct intervals over a period of ∼100 million years that migrate from the interior to the coast. A key region to help constrain the secular evolution of granitic magmatism related to the Yanshanian Orogeny is the Peal River estuary as three distinct Mesozoic magmatic belts congregate. The islands of Taipa and Coloane, Macau Special Administrative Region, are located along the western bank of the Pearl River estuary and are composed of spessartine-bearing biotite leucogranite. *In situ* zircon geochronology yielded Late Jurassic weighted-mean $^{206}Pb/^{238}U$ ages of 160.0 ± 2.0 and 161.5 ± 2.0 Ma that correlate to the late Early Yanshanian Orogeny. Inherited zircons of Middle Triassic to Middle Jurassic age were also identified. The rocks are peraluminous, ferroan, calc-alkalic to calcic and classify as post-collisional granite. Geochemical modeling indicates that the chemical variability of the rocks is related to hydrous fractional crystallization under reducing conditions (ΔFMQ −1) at ∼7 km depth. The Sr-Nd isotopes [$I_{Sr}$ = 0.71156 to 0.72477; $\varepsilon_{Nd}(t)$ = −7.9 to –8.6], zircon Hf isotopes [$\varepsilon_{Hf}(t)$ = −3.8 to −8.8], incompatible trace element ratios, and whole rock composition indicate that the parental magma was derived primarily from a sedimentary source. It is likely that the islands of Taipa and Coloane form a coherent plutonic complex that may be a member of larger batholith that extends across the Pearl River estuary to Hong Kong. The emplacement of the leucogranites is attributed to decompressional melting associated with a period of crustal relaxation or tensional plate stress that occurred during the transition from low angle subduction to high angle subduction of the Paleo-Pacific plate.

**Keywords: Early Yanshanian Orogeny, SE China, post-collisional granite, S-type granite, Cathaysia block**

## INTRODUCTION

The Mesozoic Era was a critical time in the lithotectonic development of East and Southeast Asia (Zhou and Li, 2000; Wu, 2005; Metcalfe, 2006; Zhou et al., 2006; Li et al., 2013; Shellnutt et al., 2013; Wang et al., 2013; Xu et al., 2016; Dong et al., 2018; Rossignol et al., 2018). Three major orogenic events centered around the South China Block (SCB), an amalgam of the Yangtze and Cathaysia blocks, occurred. The Early Triassic Indosinian Orogeny marks the collision between the rifted terranes of Tethyan Gondwana (e.g., Indochina, Simao) and the southern SCB (Metcalfe, 2006; Wang et al., 2013; Liu et al., 2018; Rossignol et al., 2018); in the northern SCB, the Early to Middle Triassic Qinling-Dabie orogenic belt marks the initial stages of the collision between the SCB and the North China Block (NCB) (Wu and Zheng, 2013; Dong and Santosh, 2016); and, in the east, the Early Jurassic to Late Cretaceous Yanshanian Orogeny is related to compressional-extensional cycles caused by the westward subduction of the Paleo-Pacific Ocean (Wu, 2005; Zhou et al., 2006; Li and Li, 2007; Shu et al., 2009; Dong et al., 2018). In all cases, orogenic activity was accompanied and/or followed by the emplacement of granitic plutons. However, granitic magmatism related to the Yanshanian Orogeny is unique as it lasted ∼100 million years, occurred at distinct intervals, migrated eastward, and their compositions became less aluminous over time (Zhou and Li, 2000; Zhou et al., 2006; Li et al., 2013, 2014; Shellnutt et al., 2013).

The southeastern margin of the Cathaysia Block preserves the distinct secular evolution of primarily silicic (rhyolitic and granitic), Jurassic to Cretaceous magmatic rocks associated with the Yanshanian Orogeny (**Figure 1A**). From the interior to the coast there are sub-parallel magmatic belts that decrease in age from 180−160 Ma, 160−140 Ma, to 140−90 Ma (Zhou and Li, 2000; Zhou et al., 2006; Li et al., 2013). The origin and formation of the magmatic belts is debated but, the secular evolution and the changing composition of the silicic rocks is likely related to the shift in the regional tectonic regime from the Triassic, Tethyan-controlled, Indosinian Orogeny to episodes of extension-related Early Yanshanian (180 to 142 Ma) magmatism and predominantly compression-related (142 to 67 Ma) Late Yanshanian magmatism (Zhou et al., 2006; Dong et al., 2018). Furthermore, the eastward migration of magmatism may also be related to an increase in dip angle of the westward subducting Paleo-Pacific Ocean over time (Zhou and Li, 2000; Li and Li, 2007; Jiang et al., 2009; Li et al., 2012; Zhu et al., 2014; Zuo et al., 2017).

A key region for constraining the Mesozoic tectonic evolution of SE China is the Pearl River estuary as it appears to have been the focal point of the transition from Indosinian-related orogenesis to Yanshanian-related orogenesis (**Figure 1**; Zhou et al., 2006). Thus, it is possible that periods of Yanshanian-related magmatism spatially overlap with Indosinian-related magmatism and can elucidate the importance of crustal recycling in the development and stabilization of the Cathaysia Block until the latest Cretaceous. Granitic rocks are well exposed around the coastal regions of the Pearl River estuary and there are a number of granitic islands and islets between Hong Kong and Macau that extend southward into the South China Sea (**Figures 1B,C**). The territory of Macau, located on the western bank of the Pearl River estuary is composed primarily of biotite leucogranite (Ribeiro et al., 1992; Dias et al., 2018). The leucogranites are relatively understudied but zircon U-Pb geochronology has demonstrated that they were emplaced in two separate pulses during the Jurassic (164.6 ± 0.2 to 159.3 ± 0.3 Ma, and 146.6 ± 0.2 to 140.4 ± 0.2 Ma) and contemporaneous with the late period of the Early Yanshanian Orogeny (Quelhas et al., 2020).

In this paper, we present *in situ* zircon U-Pb geochronology and Hf isotopes, mineral chemistry, whole rock geochemistry, and whole rock Sr-Nd isotopes on a collection of rocks from the Mesozoic granitic islands of Taipa and Coloane, Macau Special Administrative Region. The results of this study are used to constrain the timing, petrogenesis, and tectonomagmatic evolution of the leucogranites from southern Macau and offer new insight of the role that crustal recycling plays in the genesis of Early Yanshanian granitic magmatism within the southeastern margin of the Cathaysia Block.

## GEOLOGICAL BACKGROUND

The South China Block (SCB) is one of the largest cratons of East Asia (Wang et al., 2013). It is comprised of the Archean to Paleoproterozoic Yangtze Block in the northwest and Cathaysia Block in the southeast that were sutured together during the Neoproterozoic (900 Ma to 800 Ma), or possibly younger, Jiangnan Orogeny (Li et al., 2009; Zhao, 2015; Sun et al., 2018). The SCB is constrained by the Mesozoic Qinling-Dabie-Sulu Orogen to the north, the Indochina Block along the Ailaoshan-Song Ma suture to the south, and the Songpan-Ganzi terrane along the Longmenshan fault to the west (Wang et al., 2013).

The Cathaysia Block is separated from the Yangtze Block by the Jiangshan-Shaoxing suture and consists of Precambrian basement rocks (Neoarchean to Neoproterozoic), Sinian (∼600 Ma) to Mesozoic sedimentary and volcanic cover rocks, and extensive granitic plutons (Chen and Jahn, 1998; Xu et al., 2007; Charvet, 2013; Sun et al., 2018). During the Phanerozoic there were three regionally extensive tectonothermal events that are referred to as the "Kwangsian," "Indosinian," and "Yanshanian" (Wang et al., 2013). The Kwangsian tectonism occurred during the middle Paleozoic (Ordovician to Devonian) and largely affected the western and southern margin of the Cathaysia Block. The nature of the Kwangsian event is uncertain but is considered to be either an intracontinental deformation or a subduction-related event that led to the closure of an ocean (Wang et al., 2011). The Indosinian Orogeny occurred during the Late Permian to Late Triassic (255 Ma to 202 Ma) and is related to the collision between the Indochina block and the southern margin of SCB after the closure of the Paleotethys Ocean (Liu et al., 2018; Rossignol et al., 2018). Numerous I- and S-type granitic plutons were emplaced during this period (Chen and Jahn, 1998; Wang et al., 2013; Gao et al., 2017; Liu et al., 2018). The Yanshanian Orogeny occurred in two main stages during the Jurassic and Cretaceous and was related to subduction of the Paleo-Pacific Ocean beneath the eastern margin of Eurasia (Zhou and Li, 2000; Zhou et al., 2006; Li et al., 2013).

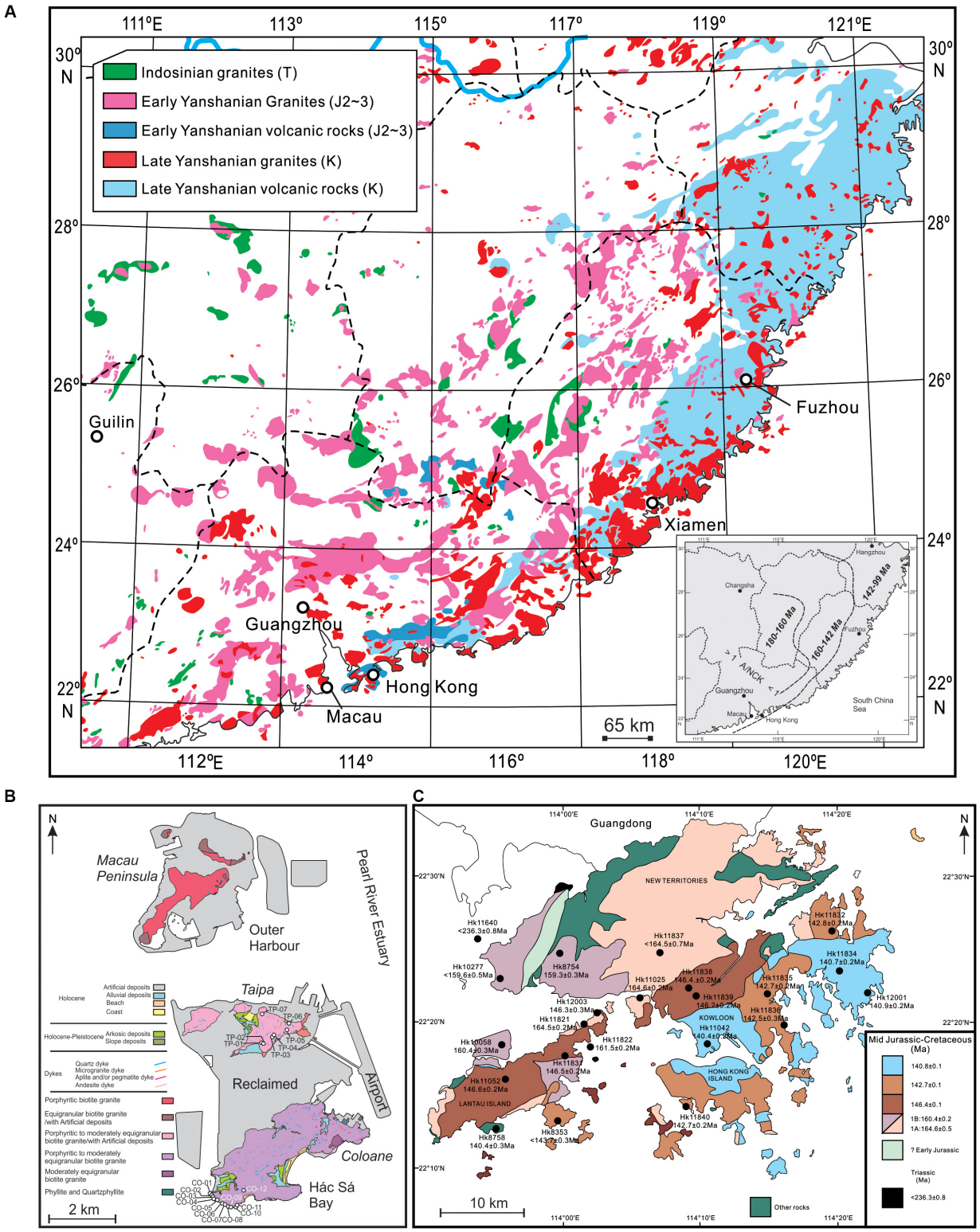


**FIGURE 1 | (A)** Regional geological map of the South China Block showing the spatial-temporal migration of Mesozoic magmatism from the interior to the coast. Inset map is of the age and compositional trend of Mesozoic volcanic and plutonic rocks of SE China. The alumina saturation index (A/NCK = Al/Na + Ca + K) of Mesozoic volcanic and plutonic rocks increases from NW to SE whereas the age decreases (Zhou et al., 2006). **(B)** Geological map of Macau Special Administrative Region showing the sample locations of this study (modified from Quelhas et al., 2020). **(C)** Geological map of Hong Kong Special Administrative Region showing locations of samples dated using high precision zircon U-Pb methods (modified from Davis et al., 1997).

The territory of Macau is located ∼65 km west of Hong Kong Island and covers an area of ∼30.5 km$^2$ (**Figures 1A,B**). It is comprised of the densely populated and urbanized Macau peninsula, and lightly populated islands of Taipa and Coloane that are connected by reclaimed land. Granite exposures on peninsular Macau are primarily exposed as small hills within city parks (Jardim Luís Camões, Parque Municipal Mong-Há, Parque Municipal do Monte Guia) or along road cuts (Estrada da Penha) at or near the southern peninsula (Ribeiro et al., 1992; Dias et al., 2018; Quelhas et al., 2020). The bedrock geology of Taipa Island is exposed primarily within forested hills of Taipa Grande and Taipa Pequena. The current and former coastal areas as well as hiking trails of Coloane are the best exposures of the bedrock in the territory of Macau. The granites observed throughout the territory are light gray to cream color, coarse grained, and granular. Microgranular and mafic enclaves as well as aplite veins were observed at many locations but may be more abundant on Coloane.

The studied samples were collected from Taipa and Coloane along two transects. Seven samples from Taipa were collected from the largest and least altered exposures along a hiking trail that encircles Parque Natural de Taipa Grande (**Figure 1B**). The exposures are mostly structureless but joints and fractures, quartz veins, and aplite dykes were observed. The rocks from Coloane were collected along the southwestern to southern coastal exposure starting at Tam Kung Temple (CO-01) and ending at Praia de Hác Sá (CO-12) along Estrada da Aldeia (**Figure 1B**). A total of fourteen samples were collected including one microgranular enclave (CO-08ME) and an aplite vein (CO-09A).

## PETROGRAPHY

The granites from Taipa and Coloane are texturally and mineralogically similar and therefore described together (**Figure 2**). The rocks are granular, coarse grained, and primarily composed of alkali feldspar (40−50 vol%), quartz (30−40 vol%), and plagioclase (10−20 vol%). Biotite (∼5 vol%) is the most common mafic mineral but there is subordinate secondary (<5 vol%) amphibole (hornblende), chlorite, and epidote. The alkali feldspar is subhedral to anhedral, and is identified by microcline twinning. Crystal boundaries tend to be irregular or serrated suggesting that it was an early formed mineral and reacted with a liquid. Quartz is typically round or sub-round and of similar size (2−3 mm) to the alkali feldspar but some crystals are smaller. Plagioclase is identified by polysynthetic twinning. It is medium to coarse grained (≤3 mm), euhedral to subhedral and has blocky to lath-like shapes with straight edge boundaries. The plagioclase and alkali feldspars are, in some cases, altered to saussurite. Biotite is medium to fine grained, interstitial to the primary minerals, has light green to light brown pleochroism, and is commonly tabular in shape with serrated crystal boundaries. Typically, biotite form clusters that have crystals of various sizes. Within or marginal to the biotite clusters is fine to medium grained garnet (<1 vol%) and xenotime (<1 vol%). Many biotite crystals have small metamict zircon. There are a few crystals of secondary hornblende but it is not a significant mineral. There is some mineral variability in abundance within and between the two islands as the rocks from Coloane tend to have very little, if any, amphibole whereas the Taipa granites tend to have accessory amounts. Apatite is present (<1 vol%) as small hexagonal crystals that are commonly associated with the biotite clusters. Subhedral to anhedral titanite (<1 vol%) and euhedral to subhedral tourmaline (<1 vol%) were identified but are relatively uncommon. There are few opaque minerals (≤1 vol%) but they are nearly always associated with altered biotite and hornblende. The opaque minerals were identified by scanning electron microscopy (SEM) as Ti-rich magnetite.

## MATERIALS AND METHODS

### Electron Probe Microanalyzer

Mineralogical investigations were executed using a field emission electron microprobe (JEOL EPMA JXA-8500F) equipped with five wave-length dispersive spectrometers (WDS). Rock specimens were sliced out within a 1-inch diameter size and mounted into epoxy resin, and then polished. Secondary- and back-scattered electron images were used to guide the analysis on target positions of minerals. A 2 μm defocused beam was operated for quantitative analysis at an acceleration voltage of 12 kV with a beam current of 6 nA. The measured X-ray intensities were corrected by ZAF-oxide method using the standard calibration of synthetic and natural chemical-known standards with various diffracting crystals, as follows: wollastonite for Si-*K*α, with TAP crystal, rutile for Ti-*K*α with PET crystal, corundum for Al-*K*α (TAP), chromium oxide for Cr-*K*α (PET), hematite for Fe-*K*α with LiF crystal, Mangum oxide for Mn-*K*α (PET), periclase for Mg-*K*α (TAP), Nickel oxide for Ni-*K*α (LiF), Zinc oxide for Zn-*K*α (LiF), wollastonite for Ca-*K*α (PET), albite for Na-*K*α (TAP), sanidine for K-*K*α (PET), fluorite for F-*K*α (TAP), and apatite for P-*K*α (PET). Peak counting times for F was 20 s, and others were 10 s, respectively. Accuracy of all standard calibrations were less than 1% and the data can be found in **Supplementary Table S1**.

### Laser Ablation ICP-MS Zircon U-Pb Dating

Samples TP-03 and CO-06 were selected for zircon separation and sent to Yu-Neng Rock and Mineral Separation Company (Lanfang, Hebei, China). Cathodoluminescence (CL) images were taken at the Institute of Earth Sciences, Academia Sinica, Taipei for examining the internal structures of individual zircon grains and selecting suitable positions for U-Pb analyses. Zircon U-Pb isotopic analyses were performed by laser ablation-inductively coupled plasma mass spectrometry (LA-ICPMS) using an Agilent 7500cx ICP-MS and a New Wave UP213 laser ablation system set up at the Department of Geosciences, National Taiwan University, Taipei, following the analytical procedure of Chiu et al. (2009). A spot size of 40 μm with laser repetition rate of 5 Hz was used and the laser energy density was ∼10 J/cm$^2$. Calibration was performed by using the zircon standard GJ-1 (608.5 ± 0.4 Ma; Jackson et al., 2004), and Plešovice (337.1 ± 0.4 Ma; Sláma et al., 2008)

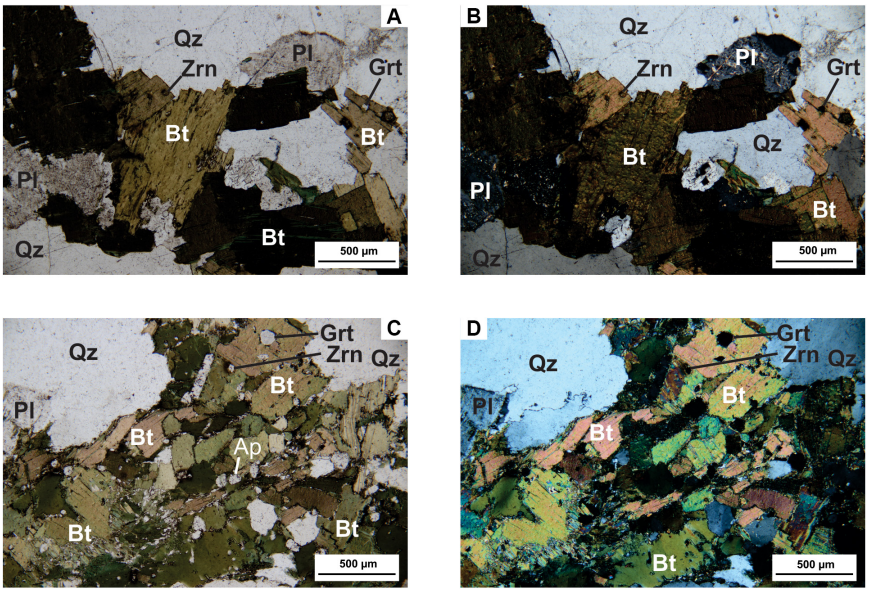


**FIGURE 2 |** Photomicrograph of the Taipa granite (TP-01) in panel **(A)** plane polarized light and **(B)** cross-polars. Photomicrograph of the Coloane granite (CO-03) in panel **(C)** plane polarized light and **(D)** cross-polars. Pl, plagioclase; Qz, quartz; Bt, biotite; Grt, garnet; Zrn, zircon; and Ap, apatite.

and 91500 (1065 Ma; Wiedenbeck et al., 1995) were used as secondary standards. Measured U-Th-Pb isotope ratios were calculated using the GLITTER 4.4 software (Griffin et al., 2008) and the relative standard deviations of reference values for GJ-1 were set at 2%. The common lead was directly corrected using the common lead correction function proposed by Andersen (2002, 2008).

The majority of the data, before common lead correction, from both samples are discordant suggesting many of the zircons, in particular the older zircons (>170 Ma) experienced Pb loss (**Supplementary Tables S2, S3**). However, the zircon $^{206}Pb/^{238}U$ ratio has nearly all of the chronometric information for Phanerozoic rocks and we interpret the emplacement age of the samples based on the weighted-mean value (Ludwig, 1998). The weighted mean U-Pb ages and Concordia plots were carried out using Isoplot v. 4.1 (Ludwig, 2011).

## Laser Ablation MC-ICP-MS Hf Isotopes

*In situ* zircon Hf isotope analyses were carried out on the same zircon spots for dating by using a Photon Machines Analyte G2 laser-ablation microprobe (193 nm, 4 ns excimer), attached to a Nu Plasma HR multi-collector ICP-MS, at the Institute of Earth Sciences, Academia Sinica in Taipei. Most analyses were carried out with a beam diameter of 50 µm, 8 Hz repetition rate, and energy of ∼8–9 J/cm$^2$. This resulted in total Hf signals of up to ∼10 V, depending on the precise conditions and Hf contents. Analyzing times were ∼2 min including 30 s of the background noise and ∼80 s of the sample intensity after laser ablation. The He carrier gas of ∼0.9 L/min (MFC1 = ∼0.7 L/min and MFC2 = ∼0.2 L/min) transported the ablated sample from the laser-ablation cell via a mixing chamber where it was mixed with Ar of ∼0.7 L/min prior to entering the ICP-MS torch. The He gas could substantially reduce the deposition of ablated material onto the sample surface and greatly improve transport efficiency, and thus increase the signal intensities. Typical within-run precision (1σ) on the analysis of $^{176}Hf/^{177}Hf$ is better than ± 0.000030, equivalent to an uncertainty of ∼1 epsilon unit. International zircon standards of Mud Tank served as the primary external reference material to monitor the condition facilities, and Plešovice, 91500, and TEMORA also served as the secondary external reference materials for data quality control. They have long-term average $^{176}Hf/^{177}Hf$ values of 0.282494 ± 28 (2σ, $n$ = 395), 0.282485 ± 28 (2σ, $n$ = 45), 0.282314 ± 23 (2σ, $n$ = 40) and 0.282689 ± 30 (2σ, $n$ = 42), respectively, all in accordance with those of 0.282504 ± 44, 0.282482 ± 13, 0.282307 ± 31 and 0.282680 ± 31 reported in Woodhead and Hergt (2005), Wu et al. (2006), and Sláma et al. (2008). All calculated data were considered for isobaric interferences and normalized to $^{179}Hf/^{177}Hf$ = 0.7325, using an exponential correction for mass bias. The Hf isotope results of the samples are presented in the online supplementary material (**Supplementary Table S4**).

## Wave-Length Dispersive X-Ray Fluorescence

For each sample, three grams (3.0000 ± 0.0005 g) was added to a ceramic crucible of known mass (+lid) and placed in an oven for 3 h at 105°C. After heating, the samples were cooled inside a desiccator for ∼15 min before they were weighed. All samples were then heated in a furnace to peak temperature of 900°C and held for 10 min before cooling. After the samples were sufficiently cooled (<200°C) they were removed from the furnace and placed in a desiccator until reaching ambient temperature. Each sample was weighed again and the loss on ignition was determined from the masses obtained

from the low and high temperature cycles. Lithium metaborate (6.0000 ± 0.0005 g) was added to the samples (0.6000 ± 0.0005 g) at a ratio of 10:1 and fused to produce a glass disc using a Claisse M4 fluxer. The major elements were measured by Panalytical Axios$^{mAX}$ WDXRF at XRF Laboratory, Department of Earth Sciences, National Taiwan Normal University. Standard reference material sample BIR-1a was measured after every five samples to track the accuracy and stability of the machine. The measured accuracy for BIR-1a is better than 5% for all elements.

## Inductively Coupled Plasma Mass Spectrometry

The glass bead used for XRF analysis for each sample (40 ± 5 mg) was decomposed in screw-top Savillex Teflon beakers containing 30 to 25 drop mixture of 1:1 nitric acid ($HNO_3$) and fluoric acid (HF). The beakers were placed on a hot plate at 140°C for 12 h. After drying of the solution, 1.5 ml $HNO_3$ was added to the dried residua. The beakers were then placed on a hot plate at 140°C for 12 h. The solution was diluted to 1500 times. The samples solution was initially diluted 500 times with 2% $HNO_3$ into 50ml bottles. The solutions were then diluted 3 times with 2% $HNO_3$ and internal standard 10 ppb (Rh + Bi) into 12ml tubes. The solutions were measured at the Institute of Earth Sciences, Academia Sinica using an Agilent 7500cx mass spectrometer. Measured standard reference materials for this study (BCR-2, BHVO-2, AGV-2, and DNC-1) and their recommended values are found in **Table 1**.

## Thermal Ionization Mass Spectrometry

Five samples (TP-02, TP-05, TP-07, CO-05, and CO-12) were measured for Sr isotopes using a Finnigan MAT-262 TIMS at the Mass Spectrometry Lab, Institute of Earth Sciences, Academia Sinica, Taipei. Approximately 100 mg of each sample powder was added to a Teflon beaker with 50 drops of concentrated $HNO_3$ and HF. The mixture was heated to 100°C for 2 days and then dried. 2 ml of 6N HCl was added to the residua and dried. After repeating this step twice, 2 ml of 1N HCl was added to the residua and then centrifuged for 10 min to congregate the supernatant. Chromatographic/column separation was used to isolate Sr from all other elements. The first column isolated the Sr and REEs using a polyethylene column (23 mm length × 5 mm in diameter) with 2.5 ml of cation exchange resin (sulfonated polystyrene resin, BioRad AG 50W-X8, Analytical Grade, 100−200 mesh). Strontium was further purified by passing through a cation exchange resin bed polyethylene column (23 mm length × 5 mm in diameter) filled with 1 ml of AG50W-X8. For the Sr isotopic measurement, the samples were loaded with $H_3PO_4$ on treated single rhenium filament. $^{87}Sr/^{86}Sr$ ratios were normalized to $^{86}Sr/^{88}Sr = 0.1194$. The 2σ external precision ($2\sigma_m$) for all samples is ≤0.000013 (**Table 2**). The certified standard NBS987 was used to ensure quality both as an internal standard and as a check for instrumental functionality. Analyses of NBS987 during the study period yielded $^{87}Sr/^{86}Sr$ ratio of 0.710248 ± 21.

Additional samples were measured for Sr (TP-04, CO-08, and CO-11) and Nd (TP-02, TP-04, TP-07, CO-05, CO-08, and CO-11) isotopes at Activation Laboratories, Ancaster, Ontario. The Sr isotopic compositions were measured in static mode by multicollector inductively coupled plasma mass spectrometry (MC-ICP-MS), and are normalized for variable mass fractionation to a value of 0.1194 for $^{86}Sr/^{88}Sr$ using the exponential law. All analyses reported here are presented relative to an $^{87}Sr/^{86}Sr$ value of 0.710245 for the NIST SRM987 international Sr isotope standard. The rock powders were accurately weighed and dissolved in mixed 24N HF + 16N HNO3 media in sealed PFA Teflon vessels at 160°C for 6 days. The fluoride residue is converted to chloride with HCl, and Nd and Sm are separated by conventional cation and HDEHP-based chromatography (Creaser et al., 1997; Unterschutz et al., 2002). The isotopic composition of Nd is determined in static mode by MC-ICP-MS (Schmidberger et al., 2007). All isotope ratios are normalized for variable mass fractionation to a value of $^{146}Nd/^{144}Nd = 0.7219$ using the exponential fractionation law. Using the same isotopic analysis and normalization procedures above, the Geological Survey of Japan Nd isotope standard "Shin Etsu: J-Ndi-1" was measured for this study (Tanaka et al., 2000) and has a $^{143}Nd/^{144}Nd$ value of 0.512107 ± 7 relative to a LaJolla $^{143}Nd/^{144}Nd$ value of 0.511850, when normalized to $^{146}Nd/^{144}Nd = 0.7219$.

# RESULTS

## Mineral Chemistry

The composition of biotite was calculated into cation proportions using the method of Tindle and Webb (1990). Following the cation calculation, the total Fe was recalculated into $Fe^{2+}$ and $Fe^{3+}$ using charge balance (Nenova, 1997). The biotite crystals from both islands are siderophyllite but only five analyses classify as primary magmatic whereas the other analyses fall within the domain of re-equilibrated biotite (Nachit et al., 2005). The Fe/(Fe + Mg) ratios are high and range from 0.72 to 0.78 but the $TiO_2$ tends to be higher in the biotite from Taipa whereas the $Al_2O_3$ (14.26 wt% to 16.88 wt%) tends to be lower ($Al_2O_3$ = 16.57 wt% to 17.71 wt%) compared to the biotite from Coloane (**Supplementary Table S1**).

Garnet is present as an accessory mineral within some samples. The cations and garnet end-member compositions were calculated using the method of Locock (2008). Analysis of three crystals shows that the garnet is spessartine (**Supplementary Table S1**). The spessartine component of the garnet ranges from 45.5 to 51.4 with the almandine component ranging from 19.5 to 23.5, and the grossular component ranges from 23.4 to 27.5. The andradite (3.0 to 3.8) and pyrope (0.1 to 0.2) components are minor.

## *In situ* Zircon U-Pb Ages

Individual zircon grains from the Taipa (TP-03) leucogranite (22°9′22.12″N, 113°33′59.85″E) are ∼100 μm × ∼300 μm (**Supplementary Figure S1**). The majority (22 of 28) of the zircons have euhedral prismatic shapes that are similar to the

**TABLE 1 |** Whole-rock chemical composition of the leucogranites from Taipa and Coloane.

| **Sample** | **TP-01** | **TP-02** | **TP-03** | **TP-04** | **TP-05** | **TP-06** | **TP-07** | **CO-01** | **CO-02** |
|---|---|---|---|---|---|---|---|---|---|
| **Island** | **Taipa** | **Taipa** | **Taipa** | **Taipa** | **Taipa** | **Taipa** | **Taipa** | **Coloane** | **Coloane** |
| **Lat. (N)** | **22.1545** | **22.1543** | **22.1561** | **22.1563** | **22.1580** | **22.1600** | **22.1609** | **22.1122** | **22.1130** |
| **Lon. (E)** | **113.5638** | **113.5640** | **113.5666** | **113.5669** | **113.5688** | **113.5686** | **113.5637** | **113.5494** | **113.5499** |
| $SiO_2$ (%) | 76.43 | 75.66 | 76.59 | 76.47 | 75.15 | 75.40 | 76.31 | 78.29 | 79.08 |
| $TiO_2$ | 0.12 | 0.07 | 0.10 | 0.06 | 0.07 | 0.15 | 0.09 | 0.15 | 0.20 |
| $Al_2O_3$ | 12.85 | 12.88 | 13.18 | 12.71 | 13.71 | 13.08 | 12.79 | 11.85 | 10.87 |
| $Fe_2O_3$ | 1.55 | 1.29 | 1.33 | 0.97 | 1.05 | 1.58 | 1.01 | 1.57 | 1.99 |
| MnO | 0.07 | 0.10 | 0.05 | 0.07 | 0.04 | 0.06 | 0.05 | 0.08 | 0.06 |
| MgO | 0.19 | 0.11 | 0.17 | 0.09 | 0.11 | 0.24 | 0.10 | 0.25 | 0.36 |
| CaO | 1.03 | 0.80 | 1.04 | 0.75 | 0.75 | 1.22 | 0.77 | 1.09 | 1.13 |
| $Na_2O$ | 3.37 | 3.67 | 3.33 | 3.66 | 3.68 | 3.33 | 4.33 | 3.15 | 2.75 |
| $K_2O$ | 4.27 | 4.39 | 4.70 | 4.30 | 5.05 | 4.30 | 3.50 | 3.03 | 2.91 |
| $P_2O_5$ | 0.02 | 0.01 | 0.02 | 0.01 | 0.01 | 0.03 | 0.01 | 0.04 | 0.04 |
| LOI | 0.40 | 0.53 | 0.42 | 0.87 | 0.57 | 0.57 | 0.66 | 0.85 | 0.84 |
| TOTAL | 100.31 | 99.50 | 100.93 | 99.95 | 100.18 | 99.97 | 99.62 | 100.36 | 100.22 |
| Mg# | 19.6 | 14.2 | 19.9 | 14.9 | 16.8 | 23.2 | 16.5 | 24.3 | 26.2 |
| Sc (ppm) | 15.9 | 10.9 | 14.3 | 16.7 | 21.8 | 17.3 | 22.8 | 22.1 | 25.3 |
| V | 7.4 | 2.0 | 5.0 | 1.4 | 3.1 | 8.8 | 0.9 | 7.2 | 12.3 |
| Cr | | | 1.4 | 1.2 | 0.1 | 0.8 | | 1.1 | |
| Co | 1.2 | 0.7 | 1.0 | 0.5 | 0.7 | 1.5 | 0.4 | 1.7 | 2.0 |
| Ni | 3.1 | 2.4 | 0.5 | 1.5 | 7.7 | 1.0 | 2.0 | 5.1 | 1.1 |
| Cu | 3.8 | 3.7 | 3.0 | 3.9 | 2.9 | 2.3 | 2.6 | 5.4 | 2.6 |
| Zn | 38.5 | 37.9 | 43.0 | 27.9 | 24.4 | 23.2 | 18.7 | 37.9 | 48.5 |
| Ga | 16.8 | 18.9 | 16.1 | 18.4 | 17.7 | 17.3 | 18.0 | 16.1 | 15.5 |
| Rb | 276 | 412 | 255 | 383 | 357 | 277 | 297 | 221 | 229 |
| Sr | 76.0 | 28.5 | 80.8 | 34.2 | 76.7 | 110 | 56.6 | 110 | 102 |
| Y | 49.9 | 124 | 23.7 | 123 | 51.1 | 51.8 | 103 | 26.2 | 65.2 |
| Zr | 116 | 110 | 88 | 71 | 81 | 116 | 93 | 113 | 145 |
| Nb | 20.6 | 34.6 | 14.1 | 26.8 | 11.9 | 20.8 | 44.2 | 18.4 | 20.3 |
| Cs | 10.2 | 23.5 | 7.7 | 9.1 | 9.9 | 13.4 | 7.4 | 8.4 | 10.1 |
| Ba | 148 | 43 | 205 | 37 | 195 | 233 | 37 | 142 | 188 |
| La | 30.1 | 11.3 | 19.3 | 10.8 | 14.1 | 33.6 | 12.6 | 27.7 | 35.3 |
| Ce | 64.3 | 26.4 | 43.6 | 27.0 | 31.8 | 66.9 | 37.3 | 59.6 | 58.4 |
| Pr | 7.83 | 3.85 | 5.15 | 3.90 | 4.11 | 8.13 | 4.40 | 7.14 | 8.42 |
| Nd | 29.4 | 16.9 | 19.36 | 17.4 | 16.7 | 29.7 | 19.0 | 26.2 | 30.8 |
| Sm | 7.03 | 7.43 | 4.75 | 8.04 | 5.50 | 6.70 | 8.35 | 5.83 | 7.40 |
| Eu | 0.45 | 0.22 | 0.49 | 0.18 | 0.44 | 0.64 | 0.23 | 0.56 | 0.60 |
| Gd | 7.03 | 11.91 | 4.17 | 12.28 | 6.08 | 6.97 | 12.18 | 4.95 | 7.92 |
| Tb | 1.17 | 2.39 | 0.67 | 2.40 | 1.21 | 1.18 | 2.40 | 0.78 | 1.38 |
| Dy | 7.22 | 16.81 | 3.87 | 16.14 | 7.72 | 7.32 | 16.25 | 4.44 | 8.86 |
| Ho | 1.54 | 3.74 | 0.78 | 3.48 | 1.60 | 1.58 | 3.45 | 0.88 | 1.92 |
| Er | 4.57 | 11.42 | 2.28 | 10.34 | 4.71 | 4.80 | 10.12 | 2.56 | 5.79 |
| Tm | 0.73 | 1.89 | 0.38 | 1.67 | 0.76 | 0.76 | 1.60 | 0.43 | 0.94 |
| Yb | 4.65 | 12.74 | 2.50 | 11.07 | 5.02 | 4.92 | 10.21 | 2.88 | 6.20 |
| Lu | 0.70 | 1.90 | 0.39 | 1.61 | 0.75 | 0.74 | 1.44 | 0.43 | 0.95 |
| Hf | 4.16 | 5.51 | 3.20 | 3.57 | 3.21 | 4.22 | 4.44 | 3.90 | 5.08 |
| Ta | 2.20 | 6.23 | 1.76 | 5.28 | 2.43 | 3.30 | 7.24 | 2.56 | 3.14 |
| Th | 43.0 | 35.8 | 32.9 | 27.7 | 26.4 | 32.9 | 39.0 | 37.5 | 40.8 |
| U | 13.7 | 22.9 | 6.5 | 13.7 | 8.3 | 10.6 | 12.7 | 5.3 | 8.9 |
| Eu/Eu* | 0.19 | 0.07 | 0.33 | 0.06 | 0.22 | 0.28 | 0.07 | 0.31 | 0.24 |
| $(La/Sm)_N$ | 2.8 | 1.0 | 2.6 | 0.9 | 1.7 | 3.2 | 1.0 | 3.1 | 3.1 |
| $(La/Yb)_N$ | 4.6 | 0.6 | 5.5 | 0.7 | 2.0 | 4.9 | 0.9 | 6.9 | 4.1 |

*(Continued)*

**TABLE 1 |** Continued

| **Sample** | **CO-03** | **CO-04** | **CO-05** | **CO-06** | **CO-07** | **CO-08** | **CO-08ME** | **CO-09A** | **CO-09** |
|---|---|---|---|---|---|---|---|---|---|
| **Rock** | **Coloane** | **Coloane** | **Coloane** | **Coloane** | **Coloane** | **Coloane** | **Coloane** | **Coloane** | **Coloane** |
| **Lat.** | **22.1127** | **22.1119** | **22.1119** | **22.1114** | **22.1109** | **22.1104** | **22.1104** | **22.1103** | **22.1103** |
| **Lon.** | **113.5500** | **113.5505** | **113.5512** | **113.5525** | **113.5531** | **113.5539** | **113.5539** | **113.5539** | **113.5539** |
| $SiO_2$ (%) | 76.59 | 74.23 | 73.71 | 74.96 | 75.33 | 71.28 | 74.02 | 76.55 | 76.02 |
| $TiO_2$ | 0.19 | 0.14 | 0.19 | 0.22 | 0.13 | 0.09 | 0.17 | 0.03 | 0.15 |
| $Al_2O_3$ | 12.27 | 13.58 | 12.69 | 12.02 | 13.26 | 14.30 | 13.52 | 12.83 | 13.10 |
| $Fe_2O_3$ | 1.98 | 1.51 | 2.03 | 2.27 | 1.51 | 1.20 | 1.94 | 0.98 | 1.70 |
| MnO | 0.08 | 0.06 | 0.08 | 0.08 | 0.05 | 0.04 | 0.08 | 0.03 | 0.09 |
| MgO | 0.31 | 0.23 | 0.33 | 0.37 | 0.22 | 0.14 | 0.26 | 0.04 | 0.22 |
| CaO | 1.50 | 1.17 | 1.36 | 1.39 | 1.06 | 0.97 | 1.24 | 0.73 | 1.45 |
| $Na_2O$ | 3.23 | 3.28 | 3.23 | 3.18 | 3.10 | 3.37 | 3.31 | 4.30 | 3.64 |
| $K_2O$ | 3.34 | 5.04 | 4.02 | 3.46 | 5.14 | 6.40 | 4.67 | 3.80 | 3.35 |
| $P_2O_5$ | 0.05 | 0.03 | 0.04 | 0.05 | 0.03 | 0.02 | 0.04 | | 0.03 |
| LOI | 0.63 | 0.55 | 0.61 | 0.59 | 0.51 | 0.39 | 0.56 | 0.50 | 0.37 |
| TOTAL | 100.16 | 99.81 | 98.31 | 98.59 | 100.33 | 98.21 | 99.80 | 99.77 | 100.12 |
| Mg# | 23.7 | 23.1 | 24.3 | 24.2 | 22.0 | 19.0 | 20.9 | 7.3 | 20.5 |
| Sc (ppm) | 19.9 | 15.2 | 22.7 | 15.3 | 24.9 | 15.7 | 21.3 | 21.0 | 19.7 |
| V | 12.4 | 9.2 | 11.8 | 15.6 | 6.8 | 5.4 | 8.0 | 1.0 | 6.0 |
| Cr | 0.9 | 1.1 | 3.2 | 4.0 | 1.9 | 3.6 | 3.3 | 4.0 | 2.8 |
| Co | 2.1 | 1.6 | 2.2 | 2.6 | 1.3 | 1.0 | 1.7 | 0.2 | 1.4 |
| Ni | 2.0 | 0.9 | 3.6 | 6.9 | 0.6 | 1.6 | 0.7 | 0.8 | 0.6 |
| Cu | 4.3 | 2.2 | 2.5 | 3.5 | 1.9 | 79.7 | 1.9 | 2.4 | 2.2 |
| Zn | 39.2 | 38.5 | 48.2 | 44.2 | 28.7 | 32.8 | 37.7 | 9.8 | 32.0 |
| Ga | 16.9 | 16.9 | 17.9 | 17.7 | 16.5 | 17.3 | 17.3 | 20.8 | 18.0 |
| Rb | 225 | 278 | 268 | 259 | 248 | 283 | 231 | 293 | 243 |
| Sr | 115 | 122 | 119 | 114 | 111 | 116 | 112 | 12.5 | 113 |
| Y | 39.8 | 44.5 | 54.2 | 53.0 | 35.6 | 36.2 | 35.8 | 118.2 | 49.3 |
| Zr | 142 | 110 | 138 | 165 | 138 | 105 | 152 | 99 | 138 |
| Nb | 19.0 | 15.3 | 22.4 | 24.0 | 15.3 | 10.3 | 18.1 | 78.6 | 23.7 |
| Cs | 10.7 | 7.6 | 16.2 | 11.2 | 5.2 | 6.4 | 5.1 | 8.5 | 13.7 |
| Ba | 204 | 330 | 260 | 212 | 460 | 436 | 296 | 12 | 186 |
| La | 27.4 | 21.0 | 31.0 | 27.7 | 42.7 | 41.0 | 33.5 | 6.8 | 41.6 |
| Ce | 58.1 | 44.7 | 65.8 | 59.4 | 88.2 | 84.4 | 69.5 | 17.6 | 85.7 |
| Pr | 6.94 | 5.40 | 7.87 | 7.22 | 10.10 | 9.74 | 8.13 | 2.58 | 9.98 |
| Nd | 25.9 | 20.4 | 29.2 | 27.3 | 35.8 | 34.7 | 29.5 | 11.1 | 35.9 |
| Sm | 6.24 | 5.46 | 7.30 | 7.04 | 7.39 | 7.31 | 6.57 | 5.68 | 8.13 |
| Eu | 0.58 | 0.66 | 0.62 | 0.58 | 0.75 | 0.81 | 0.71 | 0.09 | 0.65 |
| Gd | 6.11 | 6.09 | 7.57 | 7.58 | 6.31 | 6.35 | 6.09 | 8.96 | 7.63 |
| Tb | 1.01 | 1.09 | 1.31 | 1.30 | 0.99 | 1.02 | 1.00 | 1.93 | 1.27 |
| Dy | 6.09 | 6.97 | 8.12 | 8.16 | 5.77 | 5.85 | 5.82 | 14.25 | 7.59 |
| Ho | 1.25 | 1.45 | 1.69 | 1.71 | 1.17 | 1.17 | 1.20 | 3.28 | 1.56 |
| Er | 3.70 | 4.21 | 5.00 | 4.99 | 3.41 | 3.42 | 3.46 | 10.53 | 4.57 |
| Tm | 0.60 | 0.65 | 0.82 | 0.80 | 0.54 | 0.54 | 0.55 | 1.86 | 0.75 |
| Yb | 3.89 | 4.22 | 5.44 | 5.01 | 3.52 | 3.56 | 3.54 | 12.99 | 5.07 |
| Lu | 0.59 | 0.62 | 0.80 | 0.74 | 0.53 | 0.54 | 0.53 | 1.97 | 0.77 |
| Hf | 4.75 | 3.82 | 4.83 | 5.64 | 4.57 | 3.45 | 4.84 | 6.30 | 4.68 |
| Ta | 2.44 | 1.75 | 3.34 | 2.85 | 1.58 | 1.42 | 1.55 | 9.83 | 2.85 |
| Th | 36.5 | 26.5 | 24.7 | 39.6 | 40.2 | 34.4 | 29.7 | 39.3 | 35.9 |
| U | 8.8 | 9.2 | 10.1 | 10.7 | 8.6 | 6.5 | 8.0 | 39.9 | 12.1 |
| Eu/Eu* | 0.28 | 0.35 | 0.25 | 0.24 | 0.33 | 0.35 | 0.34 | 0.04 | 0.25 |
| $(La/Sm)_N$ | 2.8 | 2.5 | 2.7 | 2.5 | 3.7 | 3.6 | 3.3 | 0.80 | 3.30 |
| $(La/Yb)_N$ | 5.1 | 3.6 | 4.1 | 4.0 | 8.7 | 8.3 | 6.8 | 0.40 | 5.9 |

*(Continued)*

**TABLE 1 |** Continued

| **Sample** | **CO-10** | **CO-11** | **CO-12** | **BIR-1a** | **BIR-1a** | **BCR-2** | **BCR-2** | **BHVO-2** | **BHVO-2** |
|---|---|---|---|---|---|---|---|---|---|
| **Rock** | **Coloane** | **Coloane** | **Coloane** | **m.v.** | **r.v.** | **m.v.** | **r.v.** | **m.v.** | **r.v.** |
| **Lat. (N)** | **22.1101** | **22.1100** | **22.1137** | **(4)** | | **(2)** | | **(2)** | |
| **Lon. (E)** | **113.556** | **113.556** | **113.5579** | | | | | | |
| $SiO_2$ (%) | 78.27 | 75.07 | 75.81 | 47.34 | 47.96 | | | | |
| $TiO_2$ | 0.15 | 0.19 | 0.10 | 0.96 | 0.96 | | | | |
| $Al_2O_3$ | 11.64 | 13.05 | 13.08 | 15.31 | 15.5 | | | | |
| $Fe_2O_3$ | 1.64 | 2.10 | 1.14 | 11.11 | 11.3 | | | | |
| MnO | 0.06 | 0.08 | 0.04 | 0.17 | 0.175 | | | | |
| MgO | 0.23 | 0.28 | 0.16 | 9.55 | 9.7 | | | | |
| CaO | 1.18 | 1.41 | 0.94 | 13.18 | 13.3 | | | | |
| $Na_2O$ | 2.99 | 3.29 | 3.10 | 1.74 | 1.82 | | | | |
| $K_2O$ | 3.57 | 4.11 | 5.26 | 0.03 | 0.03 | | | | |
| $P_2O_5$ | 0.03 | 0.04 | 0.02 | 0.02 | 0.021 | | | | |
| LOI | 0.43 | 0.48 | 0.33 | | | | | | |
| TOTAL | 100.20 | 100.10 | 99.97 | | | | | | |
| Mg# | 21.9 | 21.2 | 21.8 | | | | | | |
| Sc (ppm) | 22.6 | 15.5 | 16.9 | | | 33 | 33.5 | 31 | 31.8 |
| V | 6.6 | 10.0 | 5.2 | | | 425 | 418 | 309 | 318 |
| Cr | 3.1 | 2.9 | 4.0 | | | 16 | 15.9 | 292 | 287 |
| Co | 1.3 | 1.7 | 1.0 | | | 37 | 37.3 | 44 | 44.9 |
| Ni | 1.3 | 0.6 | 0.4 | | | 14 | 12.6 | 119 | 120 |
| Cu | 1.8 | 2.9 | 2.0 | | | 22 | 19.7 | 128 | 129 |
| Zn | 32.4 | 44.9 | 22.5 | | | 132 | 130 | 105 | 104 |
| Ga | 15.3 | 17.7 | 15.5 | | | 22.1 | 22.1 | 21.4 | 21.4 |
| Rb | 219 | 237 | 246 | | | 46 | 46 | 9.5 | 9.3 |
| Sr | 88.6 | 111 | 102 | | | 337 | 337 | 388 | 394 |
| Y | 41.1 | 38.5 | 26.0 | | | 36 | 36.1 | 26.1 | 25.9 |
| Zr | 131 | 165 | 87 | | | 183 | 187 | 169 | 171 |
| Nb | 18.9 | 19.6 | 11.7 | | | 12.3 | 12.4 | 18.1 | 18.1 |
| Cs | 7.2 | 7.8 | 4.1 | | | 1.2 | 1.16 | 0.1 | 0.1 |
| Ba | 207 | 249 | 261 | | | 698 | 684 | 135 | 131 |
| La | 26.2 | 52.2 | 21.3 | | | 24.8 | 25.1 | 14.9 | 15.2 |
| Ce | 56.4 | 107.1 | 44.6 | | | 52.6 | 53.1 | 36.7 | 37.5 |
| Pr | 6.64 | 12.18 | 5.28 | | | 6.8 | 6.83 | 5.22 | 5.34 |
| Nd | 24.3 | 42.7 | 19.2 | | | 28.4 | 28.3 | 23.8 | 24.3 |
| Sm | 5.86 | 8.59 | 4.43 | | | 6.52 | 6.55 | 5.99 | 6.02 |
| Eu | 0.54 | 0.67 | 0.63 | | | 1.98 | 1.99 | 1.97 | 2.04 |
| Gd | 5.91 | 7.19 | 4.25 | | | 6.81 | 6.81 | 6.20 | 6.21 |
| Tb | 1.00 | 1.12 | 0.70 | | | 1.07 | 1.08 | 0.94 | 0.94 |
| Dy | 6.25 | 6.20 | 4.14 | | | 6.43 | 6.42 | 5.27 | 5.28 |
| Ho | 1.30 | 1.24 | 0.86 | | | 1.32 | 1.31 | 0.99 | 0.99 |
| Er | 3.89 | 3.56 | 2.49 | | | 3.64 | 3.67 | 2.52 | 2.51 |
| Tm | 0.64 | 0.57 | 0.39 | | | 0.54 | 0.534 | 0.34 | 0.335 |
| Yb | 4.29 | 3.93 | 2.65 | | | 3.39 | 3.39 | 1.98 | 1.99 |
| Lu | 0.65 | 0.61 | 0.39 | | | 0.51 | 0.505 | 0.28 | 0.275 |
| Hf | 4.64 | 5.63 | 2.96 | | | 4.91 | 4.97 | 4.39 | 4.47 |
| Ta | 2.61 | 3.13 | 1.51 | | | 0.78 | 0.79 | 1.17 | 1.15 |
| Th | 30.7 | 41.5 | 20.7 | | | 5.88 | 5.83 | 1.20 | 1.22 |
| U | 7.4 | 7.6 | 6.1 | | | 1.69 | 1.68 | 0.42 | 0.41 |
| Eu/Eu* | 0.28 | 0.25 | 0.44 | | | | | | |
| $(La/Sm)_N$ | 2.9 | 3.9 | 3.1 | | | | | | |
| $(La/Yb)_N$ | 4.4 | 9.5 | 5.8 | | | | | | |

*(Continued)*

**TABLE 1 |** Continued

| Sample | AGV-2a | AGV-2a | DNC-1 | DNC-1 |
|---|---|---|---|---|
| Rock | m.v. | r.v. | m.v. | r.v. |
| Lat. (N) | (3) | | (2) | |
| Lon. (E) | | | | |
| $SiO_2$ (%) | | | | |
| $TiO_2$ | | | | |
| $Al_2O_3$ | | | | |
| $Fe_2O_3$ | | | | |
| MnO | | | | |
| MgO | | | | |
| CaO | | | | |
| $Na_2O$ | | | | |
| $K_2O$ | | | | |
| $P_2O_5$ | | | | |
| LOI | | | | |
| TOTAL | | | | |
| Mg# | | | | |
| Sc (ppm) | 19 | 13.1 | 21 | 31.4 |
| V | 119 | 119 | 148 | 147.5 |
| Cr | 16 | 16.2 | 281 | 270 |
| Co | 16 | 15.5 | 55 | 56.8 |
| Ni | 17 | 18.9 | 247 | 247 |
| Cu | 53 | 51.5 | 97 | 99.7 |
| Zn | 87 | 86.7 | 60 | 70.1 |
| Ga | 21.0 | 20.4 | 13.7 | 14.7 |
| Rb | 67 | 67.8 | 3.6 | 4.7 |
| Sr | 658 | 660 | 152 | 144 |
| Y | 20.1 | 19.1 | 17.1 | 18.5 |
| Zr | 235 | 232 | 34.6 | 38.5 |
| Nb | 14.2 | 14.1 | 1.45 | 3.19 |
| Cs | 1.2 | 1.17 | 0.2 | 0.44 |
| Ba | 1127 | 1134 | 104 | 118 |
| La | 37.4 | 38.2 | 3.57 | 3.58 |
| Ce | 68.4 | 69.4 | 7.89 | 9.14 |
| Pr | 8.08 | 8.17 | 1.07 | |
| Nd | 30.0 | 30.5 | 4.75 | 5.2 |
| Sm | 5.45 | 5.51 | 1.37 | 1.41 |
| Eu | 1.64 | 1.55 | 0.58 | 0.59 |
| Gd | 4.57 | 4.68 | 2.09 | 2.2 |
| Tb | 0.66 | 0.65 | 0.38 | 0.42 |
| Dy | 3.50 | 3.55 | 2.72 | 3.0 |
| Ho | 0.68 | 0.68 | 0.63 | 0.44 |
| Er | 1.82 | 1.83 | 1.92 | 1.7 |
| Tm | 0.26 | 0.262 | 0.30 | 0.33 |
| Yb | 1.64 | 1.65 | 1.97 | 1.98 |
| Lu | 0.25 | 0.251 | 0.30 | 0.32 |
| Hf | 5.21 | 5.14 | 0.99 | 1.01 |
| Ta | 0.85 | 0.87 | 0.08 | 0.10 |
| Th | 6.20 | 6.15 | 0.23 | 0.22 |
| U | 1.91 | 1.89 | 0.06 | |
| Eu/Eu* | | | | |
| $(La/Sm)_N$ | | | | |
| $(La/Yb)_N$ | | | | |

*Mg# = {MgO (mol)/[MgO (mol) + FeOt (mol)]}*100. FeOt = $Fe_2O_3$t* 0.8998. Eu/Eu* = 2*$Eu_N$/($Sm_N$ + $Gd_N$). N, chondrite normalized to Sun and McDonough (1989). m.v., measured value; r.v., recommended value. Number in parentheses for standards is averaged number of analyses.*

P1, P2, P3, P4, S5, and S10 types of Pupin (1980) whereas the others are equant (AB3, AB4 types). Twelve of the twenty-eight zircons do not show internal structures in the CL images. Of the remaining zircons, some (8) have bright cores with darker rims, some (3) have bright rims and darker cores, some (3) have clear oscillatory zoning, and the remaining two zircons are unique (Corfu et al., 2003). One is equant with an off-center bright ring around a dark core and the other has an irregular dark core surrounded by a brighter oscillatory zoned rim. The size, morphology, and zonation of the zircons do not appear to show systematic age distribution. Analyses of 28 zircons yielded a total range of $^{206}Pb/^{238}U$ ages from 140 ± 5 Ma to 234 ± 5 Ma (1σ) and have Th/U ratios that range from 0.11 to 1.27. Twenty-four spot measurements of the standard reference materials (GJ-1 = 14, 91500 = 7; PLS = 3) yielded results within their certifiable $^{206}Pb/^{238}U$ ages (**Supplementary Table S2**). One zircon was analyzed in the core and two rim locations to evaluate temporal growth. Five age populations are identified based on the clustering of the ages (**Supplementary Table S2**). There are two distinct Triassic groups and two Jurassic groups (**Figure 3A**). The oldest Triassic age group is comprised of two zircons with ages of 234 ± 5 Ma (1σ). The younger Triassic ages are 207 ± 5 Ma (core analysis), 208 ± 5 Ma, and 217 ± 5 Ma (1σ). The oldest Jurassic ages are 172 ± 4 Ma, 173 ± 5 Ma (rim), 169 ± 4 Ma, and 169 ± 4 Ma (1σ). The largest age group ranges from 166 ± 4 Ma to 156 ± 4 Ma (1σ) and has a weighted-mean $^{206}Pb/^{238}U$ age of 160.0 ± 2.0 Ma (2σ, $n$ = 16). The weighted-mean age is within uncertainty of the Concordia intercept age of 159.5 ± 2.4 Ma. Four zircons yielded Late Jurassic to Early Cretaceous ages (153 ± 5 Ma, 140 ± 5 Ma, 144 ± 4 Ma, 145 ± 4 Ma, 1σ) but they are more discordant than the Oxfordian zircons suggesting they experienced lead loss. One zircon yielded a $^{206}Pb/^{238}U$ age of 168 ± 6 Ma (1σ) Ma but has a comparatively large measured uncertainty in the $^{207}Pb/^{235}U$ ratio.

Individual zircon grains of the Coloane (CO-06) leucogranite (22°6′40.27″N, 113°33′8.82″E) are similar in size and shape of those from TP-03 (**Supplementary Figure S2**). Twenty-five of thirty zircons from CO-06 are euhedral to subhedral, prismatic, and similar to the P1, P2, P3, P4, S5, and S10 types of Pupin (1980). The remaining five zircons are sub-round to equant in shape and resemble the AB3, AB4, and G2 types of Pupin (1980). Eight of the thirty zircons do not show internal structures in the CL images. Of the remaining zircons, some have bright cores with darker rims, one has a bright rim and darker core, and some have obvious oscillatory zoning (Corfu et al., 2003). Similar to the zircons from TP-03, the size, morphology, and zonation of the zircons do not appear to show an age correlation. Analyses of 30 zircons yielded a total range of $^{206}Pb/^{238}U$ ages from 141 ± 5 Ma to 234 ± 6 Ma (1σ) and have Th/U ratios that range from 0.12 to 0.67. Seventeen spot measurements of the standard reference materials (GJ-1 = 11, 91500 = 5; PLS = 1) yielded results within their certifiable $^{206}Pb/^{238}U$ ages (**Supplementary Table S3**). Four population clusters are identified in this sample but they are similar to TP-03 (**Supplementary Table S3**). There is one Triassic group and two Jurassic groups, and one Cretaceous group (**Figure 3B**). The Triassic group is comprised of two zircons with ages of 222 ± 12 Ma and 234 ± 6 Ma (1σ). The older Jurassic zircons range in age from 168 ± 4 Ma to

**TABLE 2** | Sr and Nd isotopes of the leucogranites from Taipa and Coloane.

| Sample | Rb (ppm) | Sr (ppm) | $(^{87}Rb/^{86}Sr)_m$ | $(^{87}Sr/^{86}Sr)_m$ | 2σ | $I_{Sr}$ | Sm (ppm) | Nd (ppm) | $(^{147}Sm/^{144}Nd)_m$ | $(^{143}Nd/^{144}Nd)_m$ | 2σ | $\varepsilon_{Nd}(t)$ | $T_{DM}$ (Ma) |
|---|---|---|---|---|---|---|---|---|---|---|---|---|---|
| TP-02 | 412 | 28.5 | 42.293 | 0.82217 | 9 | 0.72477 | 7.4 | 16.9 | 0.2658 | 0.512306 | 8 | −7.9 | |
| TP-04 | 383 | 34.2 | 32.675 | 0.79412 | 5 | 0.71887 | 8.0 | 17.4 | 0.2793 | 0.512291 | 7 | −8.5 | |
| TP-05 | 357 | 76.7 | 15.518 | 0.74696 | 7 | 0.71583 | | | | | | | |
| TP-07 | 297 | 56.6 | 15.249 | 0.75284 | 13 | 0.71772 | 8.4 | 19.0 | 0.2657 | 0.512272 | 6 | −8.6 | |
| CO-05 | 268 | 119 | 6.529 | 0.72838 | 6 | 0.71334 | 7.3 | 29.2 | 0.1511 | 0.512152 | 8 | −8.5 | 2420 |
| CO-08 | 283 | 116 | 7.074 | 0.73003 | 3 | 0.71374 | 7.3 | 34.7 | 0.1274 | 0.512139 | 7 | −8.3 | 1780 |
| CO-11 | 237 | 111 | 6.188 | 0.72581 | 2 | 0.71156 | 8.6 | 42.7 | 0.1216 | 0.512131 | 6 | −8.3 | 1683 |
| CO-12 | 246 | 102 | 6.992 | 0.72901 | 11 | 0.71291 | | | | | | | |

*m, measured. Rb, Sr, Sm, and Nd concentrations were obtained by ICP-MS and the precisions are better than ± 2%.* $T_{DM}$*-1 = (1/λ)*ln[1 + (($^{143}Nd/^{144}Nd)_m$-0.51315)/(($^{147}Sm/^{144}Nd)_m$-0.2137)]; λ = 0.00654 Ga$^{-1}$.*

187 ± 7 Ma (1σ) and have a weighted-mean $^{206}Pb/^{238}U$ age of 174.7 ± 2.7 Ma (2σ, *n* = 11). The largest group has ages ranging from 167 ± 4 Ma to 155 ± 4 Ma (1σ) with a weighted-mean $^{206}Pb/^{238}U$ age of 161.5 ± 2.0 Ma (2σ, *n* = 15). The Concordia intercept age (162.2 ± 2.5 Ma) is within uncertainty of the weighted-mean age. One zircon has an Early Cretaceous age (141 ± 5, 1σ) and another yielded a $^{206}Pb/^{238}U$ age of 161 ± 7 Ma (1σ) Ma but has a comparatively large measured uncertainty in the $^{207}Pb/^{235}U$ ratio.

## *In situ* Zircon Hf Isotopes

Zircon Hf isotopes were measured on the same spots as the crystals for U-Pb geochronology of samples TP-03 and CO-06. Not all zircons were able to yield results as some crystals were almost entirely ablated during the U-Pb measurement. The entire dataset can be found in the **Supplementary Table S4** of the online supplementary material. The Lu-Hf isotope system is more stable than the U-Pb isotope system due to the higher retentivity of Hf, Lu and U than Pb in zircon. Consequently, this may cause the zircons with ancient ages and/or those that experienced metamorphism to have suffered Pb loss (Zeh et al., 2007; Guitreau et al., 2012). For the older zircons, the calculated initial Hf isotopic values would be incorrect if using underdetermined ages. Here, we used the individual zircon $^{206}Pb/^{238}U$ ages presented above to calculate the initial $\varepsilon_{Hf}(t)$ values.

Eleven of the 30 zircons analyzed for U-Pb dating from Taipa (TP-03) yielded results. The zircons range in age from 173 ± 5 Ma (1σ) to 156 ± 4 Ma (1σ) and the time integrated ratios were calculated to the age reported for each individual zircon. The $^{176}Hf/^{177}Hf(t)$ ratios range from 0.282479 to 0.282579 and correspond to $\varepsilon_{Hf}(t)$ values from −3.0 to −7.4. The $T_{DM1}$ ages range from 985 Ma to 1109 Ma whereas the $T_{DM2}$ ages range from 1411 Ma to 1678 Ma (**Supplementary Table S2**).

Half (15 of 30) of the zircons from Coloane analyzed for U-Pb dating were measured for Hf isotopes. The zircons range in age from 176 ± 5 Ma (1σ) to 156 ± 4 Ma (1σ) and the time integrated ratios were calculated to the age reported for each individual zircon. The time integrated $^{176}Hf/^{177}Hf(t)$ ratios range from 0.282428 to 0.282533 with corresponding $\varepsilon_{Hf}(t)$ values from −5.1 to −8.2. The $T_{DM1}$ ages range from 1043 Ma to 1196 Ma with the $T_{DM2}$ ages range from 1535 Ma to 1770 Ma (**Supplementary Table S3**).

## Major and Trace Elemental Geochemistry

The major and trace elemental results are summarized in **Table 1**. The $SiO_2$ contents of the rocks range from ∼71.3 wt% to ∼79.1 wt%. The rocks are chemically ferroan (Fe* = 0.83 to 0.96), peraluminous (A/CNK = 1.0 to 1.1), and calc-alkalic to calcic (**Figure 4**; Frost et al., 2001). The rocks from Taipa and Coloane are broadly similar in composition. The rocks are more potassic than sodic as their $K_2O/Na_2O$ ratios tend to be >1 but there are six samples that have a ratio close to or below 1. The Mg# of the rocks is generally between ∼15 and ∼26 but there are two samples with low values (∼14 and ∼7). The $TiO_2$, MnO, and $P_2O_5$ are all <0.25 wt%. All rocks have normative

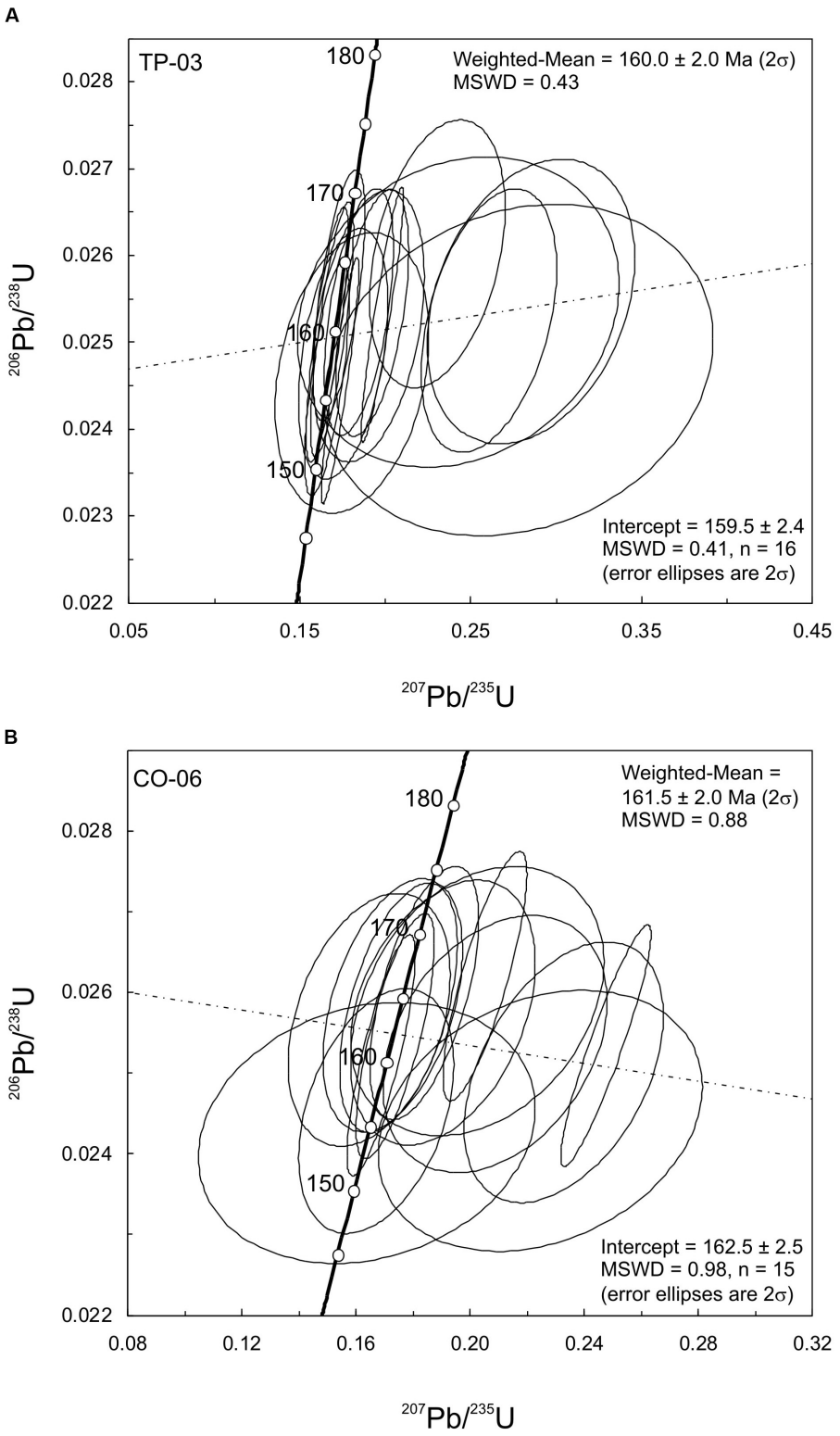


**FIGURE 3 | (A)** Concordia diagram with the weighted-mean age of zircon U-Pb data from TP-03. **(B)** Concordia diagram with the weighted-mean age of zircon U-Pb data from CO-06.

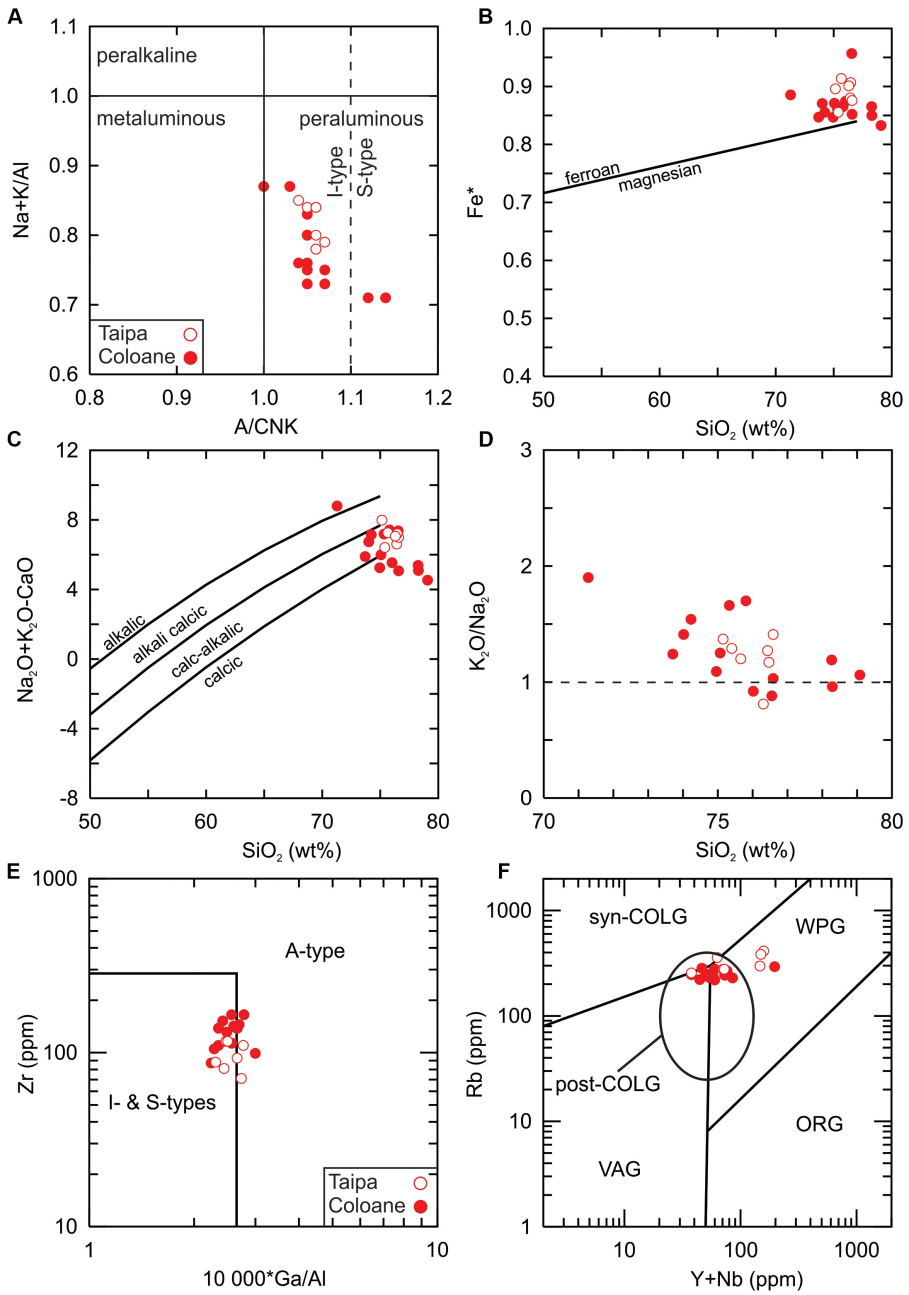


**FIGURE 4 |** Major element classification plots of the leucogranites from Taipa and Coloane. **(A)** Alkali index (Na + K/Al) vs. aluminum saturation index (ASI = Al/Ca + Na + K). Classification of the granites according to scheme of Frost et al. (2001) using **(B)** the Fe* [FeOt/(FeOt + MgO)] value and **(C)** the modified alkali-lime index ($Na_2O + K_2O$-CaO) vs. $SiO_2$ (wt%). **(D)** $K_2O/Na_2O$ vs. $SiO_2$ showing the potassic nature of the rocks. **(E)** Tectonomagmatic discrimination of granitic rocks using the criteria of Whalen et al. (1987). **(F)** Classification of granitic rocks using Rb (ppm) vs. Y + Nb (ppm) of Pearce (1996). Syn-COLG, syn-collisional granite; WPG, within-plate granite; VAG, volcanic-arc granite; ORG, ocean-ridge granite; post-COLG, post-collisional granite.

quartz, plagioclase, orthoclase, corundum, hypersthene, ilmenite, magnetite, and apatite. The normative corundum is between ∼0.1 and ∼1.5 vol% which straddles the divide between the classification of I-type and S-type granite (Chappell and White, 1974). The low loss on ignition values (<0.9%) suggests the rocks did not experience significant post-emplacement hydrothermal alteration. Tectonomagmatic discrimination diagrams indicate the rocks straddle the boundary between within-plate (A-type) and volcanic-arc (I-type) granites suggesting they may be similar to post-collisional granites (**Figures 4E,F**; Whalen et al., 1987; Pearce, 1996).

The trace element compositions of Taipa and Coloane are characterized by low concentrations of transition metals with Sc (∼10 to ∼25 ppm), V (≤16 ppm), Cr (≤4 ppm), Co

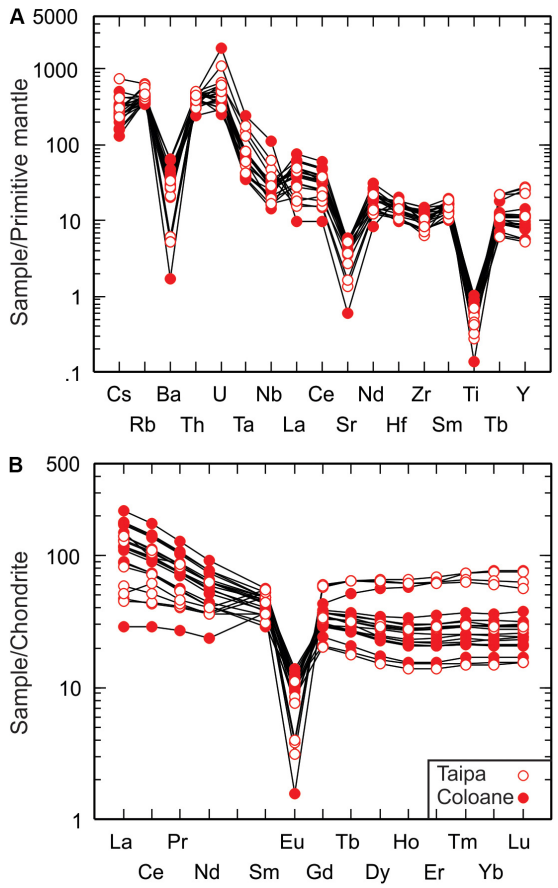


**FIGURE 5 | (A)** Primitive-mantle normalized incompatible element and **(B)** chondrite normalized rare earth element diagrams of the leucogranites from Taipa and Coloane. Rocks are normalized to values of Sun and McDonough (1989).

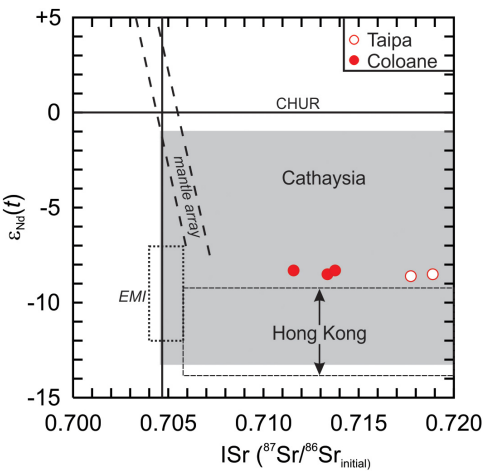


**FIGURE 6 |** Age corrected Sr-Nd isotopes of the leucogranites from Taipa and Coloane. Range of granitic rocks from the Cathaysia Block in gray (Chen and Jahn, 1998). The Sr-Nd range of Jurassic granitic rocks from Hong Kong (HK) from Darbyshire and Sewell (1997). EMI = enriched mantle I (Zindler and Hart, 1986); CHUR = chondrite uniform reservoir.

(≤3 ppm), and Ni (≤7 ppm) all less than 30 ppm. The contents of Rb (219 to 412 ppm), Zr (71 to 165 ppm), Sr (28 to 122 ppm), and Ba (43 to 460 ppm) are high and somewhat variable. The Th (20 to 43 ppm) and U (5 to 40 ppm) contents are relatively high compared to average upper crust values (Th = 10.5 ppm; *U* = 2.7 ppm; Rudnick and Gao, 2003). The primitive mantle normalized incompatible patterns of all rocks are similar with negative anomalies of Ba, Nb, Sr and Ti (**Figure 5A**). The chondrite normalized rare earth element (REE) patterns (**Figure 5B**) are more variable with depleted to enriched $La_N/Sm_N$ (0.8-3.9) ratios and flat to enriched heavy REE patterns ($Gd_N/Yb_N$ = 0.6−1.5). All samples have negative Eu-anomalies ($Eu/Eu^*$ = 0.07 to 0.44).

## Sr-Nd Isotope Geochemistry

A total of eight samples were selected for Sr isotopic analysis whereas six were selected for Nd isotopic analysis (**Table 2**). The initial Sr ($I_{Sr}$) and Nd isotope ratios were calculated to the emplacement age of 162 Ma. The $I_{Sr}$ of the granites shows a wide range from 0.71156 to 0.72477. The large range is likely due to error propagation related to some samples having high (>10) $^{87}Rb/^{86}Sr$ ratios (Jahn, 2004). In fact, the rocks from Taipa have the highest $^{87}Rb/^{86}Sr$ ratios (13.518 to 42.293) and the widest $I_{Sr}$ range (0.009) whereas the rocks from Coloane have lower and more restricted $^{87}Rb/^{86}Sr$ ratios (6.188 to 7.074) and a narrower $I_{Sr}$ range (0.002). Consequently, the Sr isotopic values from Coloane are probably more indicative of the magma source (**Figure 6**). The initial $^{143}Nd/^{144}Nd$ ratios have a relatively narrow range (0.511990 to 0.512024) across all samples. The corresponding $\varepsilon_{Nd}(t)$ values range from −7.9 to −8.6 assuming a $^{147}Sm/^{144}Nd$ ratio of 0.1967 and $CHUR_{today}$ value of 0.512638. There is no significant difference between the rocks from Taipa and Coloane. The $T_{DM}$ ages range from 2420 Ma to 1683 Ma for the samples with $^{147}Sm/^{144}Nd$ ratios < 0.165.

# DISCUSSION

## Emplacement Age and Inheritance Within the Pearl River Estuary Granites

The rocks of Macau, Taipa and Coloane were dated by isotope dilution (ID) TIMS and laser ablation multi-collector ICP-MS (Quelhas et al., 2020). The ages cluster into two distinct populations. The older rocks from Taipa and Coloane are Oxfordian (164.5 ± 0.6 Ma to 162.9 ± 0.7 Ma) whereas the younger rocks from peninsular Macau are Kimmeridgian (156.6 ± 0.2 Ma to 155.5 ± 0.8 Ma). Two dykes that intrude Taipa (~150 Ma) and Coloane (<119.7 ± 0.1 Ma) yielded the youngest ages. The zircon geochronology results from this study yielded ages within uncertainty of the TIMS ages for Taipa and Coloane. Sample TP-03 yielded a weighted-mean $^{206}Pb/^{238}U$ age of 160.0 ± 2.0 Ma whereas CO-06 yielded an age of 161.5 ± 2.0 Ma. All of the reported ages indicate that magmatism in Macau corresponds to the early period of the Yanshanian

Orogeny although the Kimmeridgian rocks probably indicate the waning stages of magmatism.

Across the Pearl River estuary, detailed geochronology and geochemical investigations of the silicic rocks of Hong Kong show that the majority of granites and rhyolites were emplaced during two periods: (1) 164.6 ± 0.2 Ma to 159.3 ± 0.3 Ma, and (2) 146.6 ± 0.2 Ma to 140.4 ± 0.2 Ma with two minor intrusions emplaced at 151.9 ± 0.2 Ma to 148.1 ± 0.2 Ma (Davis et al., 1997; Sewell et al., 2012). Moreover, the rocks show a compositional evolution from calc-alkaline, through high-K calc-alkaline, to transitional shoshonite that is thought to be related to a change in the tectonic regime from subduction-related to extension-related (Sewell and Campbell, 1997). The Oxfordian ages of Taipa and Coloane are within the uncertainty of ages reported from the period 1 (164.6 ± 0.2 Ma to 159.3 ± 0.3 Ma) granites of Hong Kong suggesting there could be a voluminous, contiguous batholith comprised of a number of individual plutons that extends across the Pearl River estuary (Davis et al., 1997; Sewell et al., 2012). The younger ages (Tai Lam < 159.6 ± 0.5 Ma; Tsing Shan = 159.3 ± 0.3 Ma) are still ∼3 Ma older than peninsular Macau indicating there are at least three distinct Late Jurassic pulses. The relative quiescence of magmatism between the Kimmeridgian rocks and the Tithonian to Berriasian (146.6 ± 0.2 Ma to 140.4 ± 0.3 Ma) granites of Hong Kong marks the transition from the Early Yanshanian to the Late Yanshanian Orogeny and may be related to change from a flat slab collisional regime to one of back-arc extension and high angle subduction (Zhu et al., 2014).

The leucogranites from this study revealed three (2 Triassic, 1 Jurassic) distinct populations of inherited zircons. The oldest population is Carnian. The combined four zircons (2 from Taipa and 2 from Coloane) yield $^{206}Pb/^{238}U$ ages from 222 ± 12 Ma to 234 ± 6 Ma (1σ). The middle population is the smallest (3 zircons), exclusively derived from Taipa, and Norian in age. The individual ages range from 207 ± 5 Ma (2σ) to 217 ± 5 (1σ). The largest population of inherited (15) zircons are Toarcian and found in both intrusions but are more abundant in Coloane (11) relative to Taipa (4). The weighted-mean $^{206}Pb/^{238}U$ age for all Toarcian zircons is 173.4 ± 2.3Ma (2σ). One zircon included in the Toarcian age from Coloane is 187 ± 14 (1σ) and statistically anomalous. Consequently, it is likely that there is a major Middle Triassic to Early Jurassic component in the crust around the Pearl River estuary.

The three groups of inherited zircons identified in our study overlap with single ID-TIMS analysis reported from Hong Kong (192.4 ± 0.5 Ma, 181.5 ± 0.7 Ma, 176.9 ± 0.5 Ma), Taipa (172.6 ± 3.6 Ma), and Coloane (204.2 ± 0.2 Ma). Moreover, a single Middle Triassic age of <236.3 ± 0.8 Ma was reported for the two-mica Deep Bay pluton located between Hong Kong and Shenzhen (**Figure 1C**). Inherited zircons measured by *in situ* methods reported by Quelhas et al. (2020) shows there are single zircons of Toarcian, Pliensbachian, and Norian ages but also there are Devonian, Silurian, Neoproterozoic (∼900 Ma to ∼700 Ma), Mesoproterozoic (∼1100 Ma), Paleoproterozoic (∼2400 Ma) and Archean (∼3300 Ma) zircons. Thus, the formation of the granitic rocks in Hong Kong and Macau involved recycling of Early Yanshanian rocks and crustal material dating to the formation of the Cathaysia Block until their emplacement during the Oxfordian (Xu et al., 2007; Zhu et al., 2014).

## Petrogenesis of the Taipa and Coloane Granites

### Tectonomagmatic Classification

The granites from Taipa and Coloane are somewhat unusual as they tend to defy numerous granite classification schemes (**Figures 4E,F**, **7**). For example, their ASI values are mostly weakly peraluminous (A/NCK < 1.1) but there are two samples with higher values (>1.1). The division between I-type and S-type granite according to Chappell and White (2001) is ∼1.1. Moreover, all rocks have normative corundum <1%, hornblende is uncommon, $Na_2O$ tends to be but not always <3.2 wt% in rocks with ∼5 wt% $K_2O$, the rocks straddle the boundary between A-type and I- and S-type in the classification of Whalen et al. (1987), and fall along the boundary between syn-collisional, post-collisional, and within-plate granite of the Rb-Y + Nb diagram of Pearce (1996).

According to the classification scheme of Frost et al. (2001), the rocks from Taipa and Coloane are ferroan, and calc-alkalic to calcic. Rocks of this composition are considered to be generated by low pressure partial melting of the crust (Frost and Frost, 2011). A crustal origin is very likely as the isotopes, trace element ratios, and inherited zircons are all consistent with an enriched source (**Figure 6**). The petrogenesis will be discussed in more detail below but a crustal origin does not help to constrain the likely tectonic environment (i.e., compression vs. extension) during emplacement. The discrimination of granites by Maniar and Piccoli (1989) categorizes rocks into seven tectonic environments using major element data. The granites from Taipa and Coloane consistently fall within the post-orogenic granite (POG) field and the $CaO/Na_2O$ and $Al_2O_3/TiO_2$ ratios indicate the rocks are strongly peraluminous post-collisional granites (**Figures 7A–C**; Sylvester, 1998). Furthermore, the rocks are broadly similar to the high-K calc-alkaline granites (KCG) of Barbarin (1999). The KCG are described as being present in various geodynamic environments but mainly associated with the transition from compressional regimes to tensional regimes. The broad consistency between of the classification schemes of Maniar and Piccoli (1989), Pearce (1996), Sylvester (1998), Barbarin (1999) suggest the rocks were likely emplaced during a period of crustal relaxation and are best described as post-collisional granites.

### Magmatic Conditions

Common minerals (biotite, hornblende) and mineral pairs (ilmenite, magnetite) of granitic rocks can be used to estimate the thermodynamic conditions (temperature, relative oxidation state, pressure) of their crystallization (Hammarstrom and Zen, 1986; Frost et al., 1988; Shabani et al., 2003; Uchida et al., 2007; Mutch et al., 2016). The estimates can then provide constraints on the formation and evolution of their parental magma. The granitic rocks from Taipa and Coloane do not contain significant quantities of amphibole or Fe-Ti oxide minerals. However, the crystallization temperature (Luhr et al., 1984), pressure (Uchida

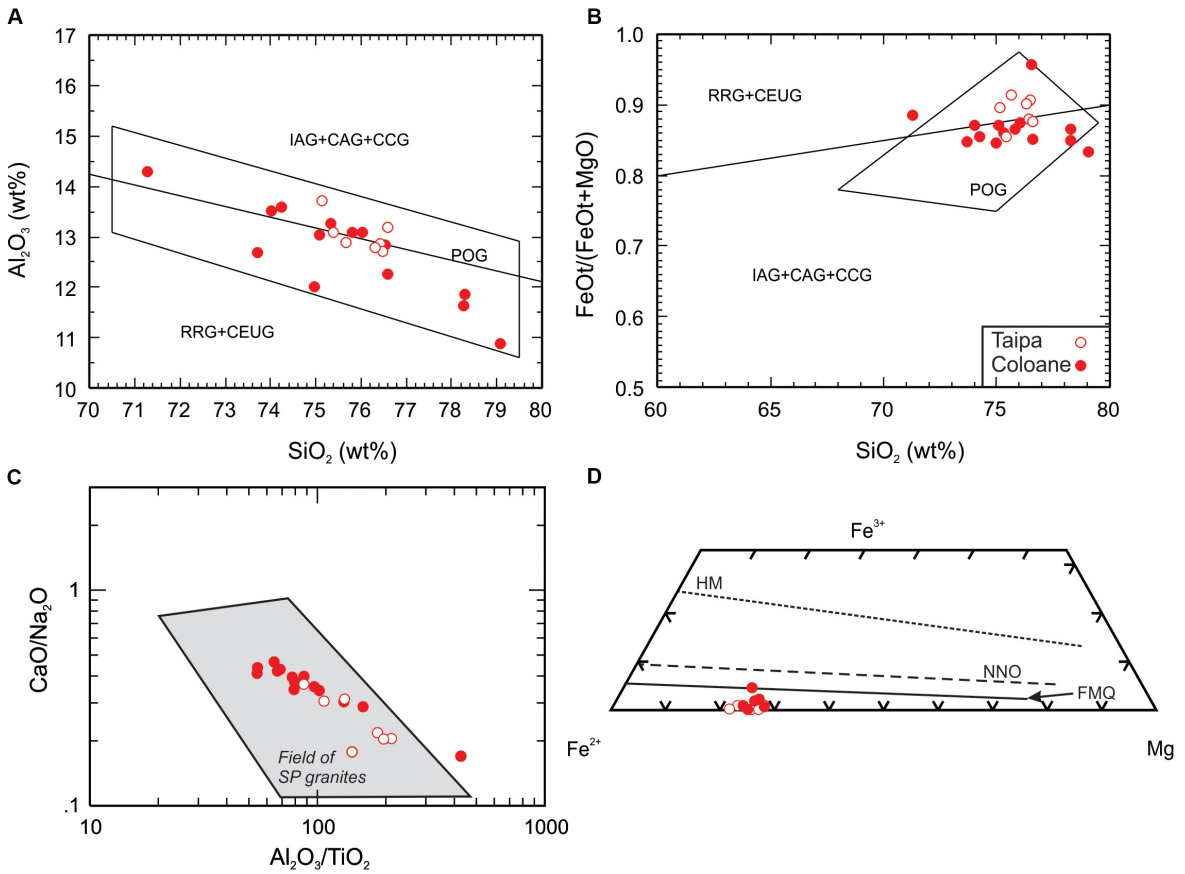


**FIGURE 7 |** Tectonomagmatic discrimination of granitic rocks and biotite composition redox estimates. **(A)** Distinction between collisional (IAG + CAG + CCG) and non-collisional (RRG + CEUG) granites using $Al_2O_3$ (wt%) vs. $SiO_2$ (wt%). **(B)** Distinction between collisional (IAG + CAG + CCG) and non-collisional (RRG + CEUG) granites of Maniar and Piccoli (1989) using FeOt/(FeOt + MgO) vs. $SiO_2$ (wt%). FeOt, total Fe expressed as $Fe_2O_3$ wt% * 0.8998. RRG, rift-related granitoids; CEUG, continental epeirogenic uplift granitoids; POG, post-orogenic granitoids; IAG, island arc granitoids; CAG, continental arc granitoids; CCG, continental collision granitoids. **(C)** $CaO/Na_2O$ vs. $Al_2O_3/TiO_2$ classification of strongly peraluminous granitic rocks. **(D)** Composition of biotite from the Taipa and Coloane leucogranites express in the $Fe^{2+}$-$Fe^{3+}$-Mg diagram from Wones and Eugster (1965). FMQ, fayalite-magnetite-quartz buffer; NNO, Ni-NiO buffer; HM, hematite-magnetite-buffer.

et al., 2007), and redox state (Wones and Eugster, 1965; Shabani et al., 2003) can be estimated based on the composition of biotite.

The crystallization temperature of biotite may be estimated in granitic rocks using the equation (1) of Luhr et al. (1984):

$$T\,(K) = \frac{838}{1.0337 - \frac{Ti}{Fe2+}} \quad (1)$$

The magmatic biotite thermometry estimates, as calculated by the equation reported, ranges from ~930 K to ~890 K (~650°C to ~610°C). The temperatures are relatively low as it is thought that granitic solidification should occur around 650°C to 700°C (Freiberg et al., 2001) but it is possible that solidification can extend to lower (<650°C) temperatures. Glazner and Johnson (2013), Challener and Glazner (2017) suggest that repeated cycles of heating and fluxing by water-rich fluids may allow the crystallization of many minerals in calc-alkalic granites to be lower than 650°C and thus consolidation temperatures may also be lower. Regardless, we think the highest biotite crystallization temperature (~650°C) is probably representative of the crystallization temperature of biotite in this system. The highest temperature (~650°C) is within the uncertainty (±40°C) of the zircon saturation temperatures ($T_{Zr}$°C = 751°C to 681°C) estimated from the whole rock data but is generally lower (Boehnke et al., 2013). The different temperature estimates between the two methods is not surprising as the crystallization temperature of zircon is variable but tends to be higher than for biotite (Harrison et al., 2007). Moreover, the inheritance-rich nature of the granites from Taipa and Coloane is consistent with the generally lower $T_{Zr}$°C values but also that it probably required fluid fluxing for melting initiation (Miller et al., 2003). Therefore it is likely that the initial magmatic temperature was generally low (e.g., ≤850°C) but closer to the highest zircon saturation temperature estimates and that biotite crystallized relatively late.

The Al-in-hornblende geobarometer is one of the few methods that can estimate crystallization pressure within granitic systems but in the absence of hornblende there are few minerals or mineral pairs that could constrain the depth of crystallization (Hammarstrom and Zen, 1986; Mutch et al., 2016). Uchida et al.

(2007) demonstrated that Al-in-biotite appears to be sensitive to pressure in a manner similar to Al-in-hornblende and is a potentially more robust geobarometer due to its ubiquity with granitic rocks (equation 2).

$$P\ (kbar) = 3.33Al^{T} - 6.53\ (\pm 0.33) \quad (2)$$

Using the equation of Uchida et al. (2007), we calculated the crystallization pressure of the magmatic biotite from this study. The pressure estimates range from 1.48 kbar to 3.28 kbar. The variability in the pressure estimates could be an artifact related to redistribution of biotite that crystallized at different pressure within the magma system during emplacement. Nevertheless, the results suggest the granites of Taipa and Coloane were emplaced between ∼5.5 km and ∼12.1 km depth.

The relative oxidation state of biotite can be estimated using the $Fe^{2+}$-$Fe^{3+}$-Mg components (Wones and Eugster, 1965; Shabani et al., 2003). The $Fe^{3+}$ content of the magmatic biotite from this study was not directly measured but was estimated using charge balance (Nenova, 1997). The results show that the biotite from Taipa and Coloane are close to the fayalite-magnetite-quartz (FMQ) buffer (**Figure 7D**). If we convert the biotite chemistry results to log $fO_2$ values using the pressure estimates then they range from −19.01 to −20.17 that is equivalent to ΔFMQ −1 (ΔFMQ = −0.96 to −1.00) and reducing conditions.

## Fractional Crystallization Modeling

The granites from Taipa and Coloane are compositionally similar and highly silicic ($SiO_2$ > 72 wt%) but there is chemical variability between the least (CO-08) silicic sample and the most (CO-02) silicic sample. However, in comparison, most ($TiO_2$, $Fe_2O_3$t, MgO, CaO, $P_2O_5$) major elements do not show clear evolutionary trends with respect to $SiO_2$ but, $Al_2O_3$, $Na_2O$, and $K_2O$ clearly decrease with increasing $SiO_2$. Given that the feldspars and quartz are the main constituents of the rocks it is likely that the negative trends of alumina and alkalis are a consequence of their crystallization. Therefore, in order to test this hypothesis we apply fractional crystallization modeling using the program MELTS (Smith and Asimow, 2005).

We use the least "evolved" composition (CO-08) as the parental magma, the redox condition and pressure estimates from the biotite mineral chemistry, and the two-feldspar mineralogy to constrain the water content. Based on the biotite composition, the redox condition used for the model is ΔFMQ -1. The pressure estimates from the biotite cover a wide range from ∼0.15 GPa to ∼0.33 GPa (∼5.5 to ∼12.1 km depth) suggesting that the plutons may have crystallized over a depth of ∼7 km. Therefore, we selected a pressure of 0.2 GPa for the model. The water content is difficult to estimate as biotite is the primary volatile-rich mineral but due to the presence of two feldspars we suggest the magma was originally water-rich and thus select near water-saturation ($H_2O$ = 4.0 wt%) conditions.

The evolution of the liquid composition is shown in **Figure 8** at 10°C intervals and the fractionation assemblage and modal proportions are summarized in **Table 3**. The entire results are in **Supplementary Table S5**. The liquidus temperature is 870°C as alkali feldspar ($An_1Ab_{24}Or_{76}$) is the first mineral to crystallize and is followed by plagioclase ($An_{22}Ab_{70}Or_8$) at 770°C, clinoamphibole (anthophyllite) at 760°C, ilmenite at 750°C, and olivine ($Fo_8$) at 730°C. As the model reaches the terminal temperature (650°C), quartz (710°C), and aluminous minerals (garnet at 670°C, cordierite at 660°C, and sillimanite at 650°C) begin to crystallize. The chemical variability of the granites is reproduced across all elements by 740°C after ∼42% fractionation composed of sodic plagioclase (∼6.1%), alkali feldspar (∼35.1%), ilmenite (∼0.04%) and clinoamphibole (∼0.8%). The modeling results indicate that the chemical variability in the granites is principally controlled by alkali feldspar and plagioclase. This is consistent with the whole rock trace element compositions as Ba, Sr, and Eu/Eu* decrease with increasing $SiO_2$. Furthermore, the results are applicable for both groups of granites (Taipa and Coloane) suggesting it is possible that they are members of the same intrusive body rather than separate plutons or magma batches.

## Magma Source

The geochemical and isotopic evidence indicates that the leucogranites are derived from the crust with limited or no input from the mantle. As discussed earlier, peraluminous, ferroan, and calc-alkalic to calcic granitoids are interpreted to be products of partial melting of quartzofeldspathic crust (Frost and Frost, 2011). The enriched whole rock Nd isotopes are consistent with a crustal source for the parental magmas of Taipa and Coloane as they overlap with the basement rocks of the Cathaysia Craton (**Figure 6**). The zircon Hf isotopes indicate there is no significant difference between the two islands although the Oxfordian zircons tend to have slighter higher $\varepsilon_{Hf}(t)$ values from Taipa (weighted-mean = −5.6 ± 0.7, 2σ) than Coloane (weighted-mean = −6.5 ± 0.6, 2σ) but the weighted-mean values are within uncertainty. The Toarcian inherited zircons from each island cannot be readily distinguished from their main Oxfordian populations suggesting the source of the two magmatic pulses was either similar or the same. Moreover, the zircon Hf crustal evolution model ages (∼1730 Ma to ∼1410 Ma) and whole rock Nd model ages (∼2420 Ma to ∼1680 Ma) are contemporaneous with a major crustal event in Cathaysia during the Paleoproterozoic (Chen and Jahn, 1998).

The primitive mantle normalized incompatible element patterns have depletions of Nb-Ta, and enrichment of Th-U that are associated with continental crust (Rudnick and Gao, 2003). Consequently, the trace element ratios such as Th/Nb, Nb/U, and Th/Yb are very high and extend beyond average upper crust values of Wedepohl (1995); Rudnick and Gao (2003) (**Figure 9**). The biotite chemistry is consistent with granitic rocks that are strongly contaminated and reduced and also within the range of S-type granites (**Figure 9**; Abdel-Rahman, 1994; Shabani et al., 2003). A crustal origin is also consistent with high Rb/Sr (2 to 46) ratios as it is similar to peraluminous low-Sr, leucogranites that are derived from melting of a metasedimentary source (**Figure 10A**; Patiño Douce, 1999; Altherr et al., 2000; Kemp and Hawkesworth, 2003). A comparison between the whole rock composition of the Taipa and Coloane leucogranites and melt compositions generated from metasedimentary and metabasaltic rocks show an affinity for a metagraywacke or a clay-rich source (**Figures 10B,C**). Furthermore, the wide age range of inherited

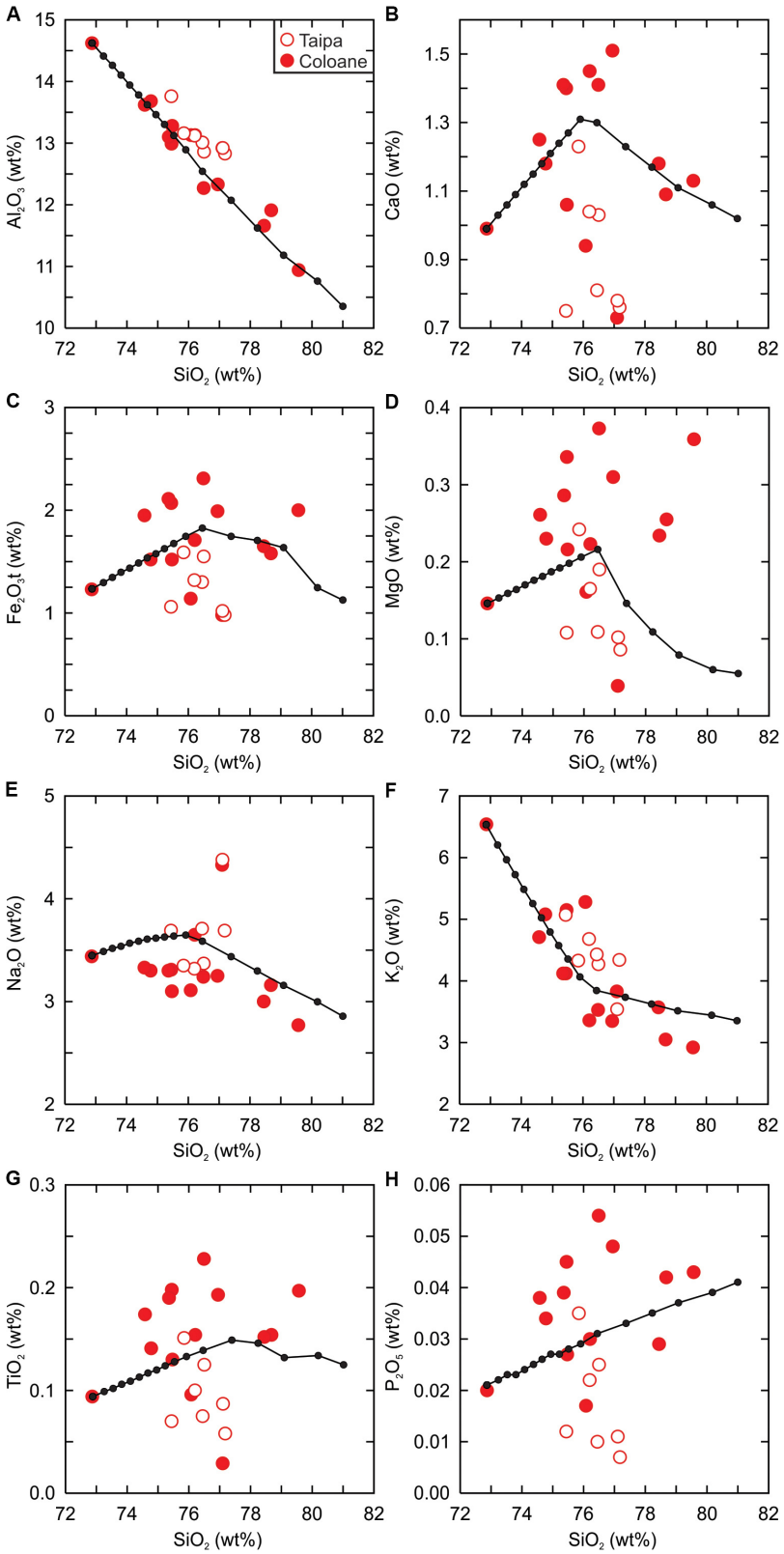


**FIGURE 8 |** MELTS fractional crystallization modeling of the leucogranites showing the major element liquid composition evolution curves. **(A)** $Al_2O_3$ (wt.%) vs. $SiO_2$ (wt%), **(B)** CaO (wt.%) vs. $SiO_2$ (wt%), **(C)** $Fe_2O_3t$ (wt.%) vs. $SiO_2$ (wt%), **(D)** MgO (wt.%) vs. $SiO_2$ (wt%), **(E)** $Na_2O$ (wt.%) vs. $SiO_2$ (wt%), **(F)** $K_2O$ (wt.%) vs. $SiO_2$ (wt%), **(G)** $TiO_2$ (wt.%) vs. $SiO_2$ (wt%), and **(H)** $P_2O_5$ (wt.%) vs. $SiO_2$ (wt%). The model shows the liquid compositions at 10°C intervals (solid black dots). All data recalculated on an anhydrous basis.

**TABLE 3 |** Summary of mineral fractionation and modes of the MELTS models.

| | FMQ−1 | | |
|---|---|---|---|
| **Mineral** | **Temp. (°C)** | **Composition** | **Modal %** |
| Afs | 870–650 | $An_1Ab_{24-22}Or_{76-78}$ | 50.2 |
| Pl | 770–650 | $An_{22-29}Ab_{70-67}Or_{8-4}$ | 19.9 |
| Il | 750–650 | | 0.2 |
| Cam | 760–750, 680 | | 0.8 |
| Ol | 730–680 | $Fo_{8-10}$ | 1.1 |
| Qz | 710–650 | | 23.7 |
| Grt | 670–650 | $Py_{13-16}Al_{80-77}Gr_{7-6}$ | 0.02 |
| Crd | 660–650 | | 0.003 |
| Sil | 650 | | 0.03 |

*Afs, alkali feldspar; Pl, plagioclase; Il, ilmenite; Cam, clinoamphibole (anthophyllite); Ol, olivine; Qz, quartz; Grt, garnet; Crd, cordierite; Sil, sillimanite. Mineral abbreviations from Whitney and Evans (2010). An, anorthite component; Ab, albite component; Or, orthoclase; Fo, forstertite component; Py, pyrope component; Al, almandine component Gr, grossular component.*

zircons favors a sedimentary source as Mesozoic sedimentary rocks deposited near the margin of Cathaysia could conceivably contain Archean (∼3300) to Phanerozoic (∼174 Ma) zircons.

Additional supporting evidence of a sedimentary source origin of the leucogranites is the presence of garnet. Garnet is a common accessory mineral within S-type granites due to excess Al in the source rocks (Sylvester, 1998; Chappell and White, 2001). The spessartines of this study are compositionally similar to magmatic garnet from silicic plutonic rocks (Miller and Stoddard, 1981). Due to the decomposition reaction of chlorite-chloritoid, almandine garnet is more common in metapelitic/metapsammitic rocks and thus is more likely to exert influence on the magma composition by increasing maficity (Mg + Fe mol/100g) and heavy rare earth element concentrations, and decreasing Si content (Stevens et al., 2007). Thus, whole rock correlations between maficity, Si (mol/100g), Ca (mol/100g), and heavy are earth elements (HREE) can indicate the influence of peritectic garnet in the magma system (Stevens et al., 2007; Villaros et al., 2009). In the case of Taipa and Coloane, it appears that peritectic garnet was not an influence in the magma system as maficity does not significantly increase with decreasing Si, or increasing Ca and HREE (**Figure 11**). The implication is that the source rocks did not likely contain garnet and that they were no deeper than ∼10 km depth (≤0.3 GPa) and experienced a maximum metamorphic facies of hornfels before

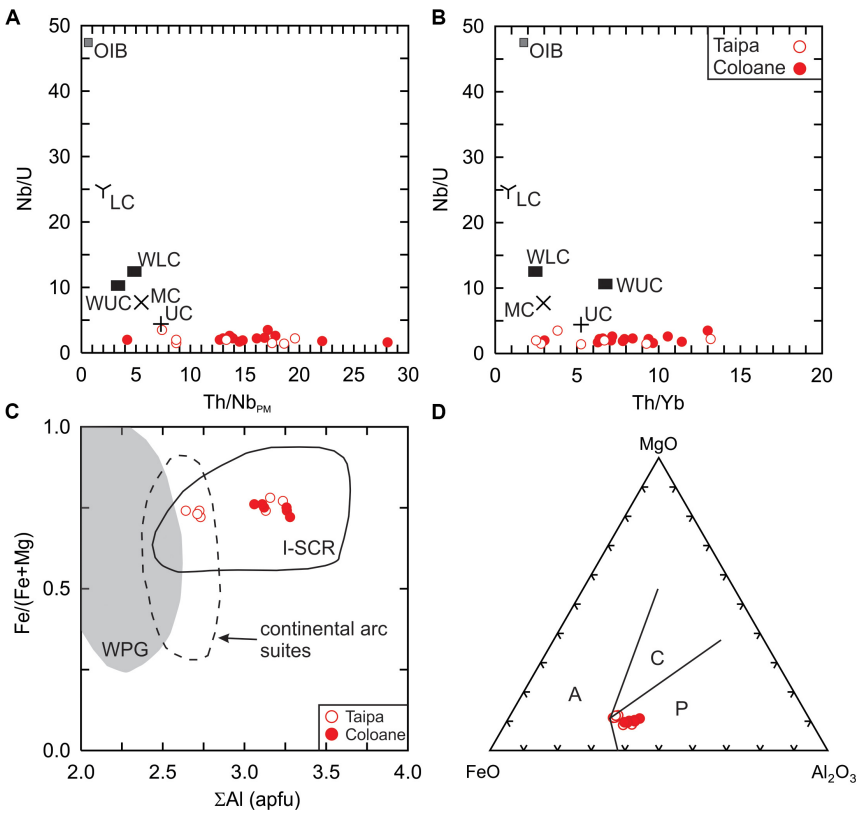


**FIGURE 9 | (A)** Nb/U vs. Th/NbPM and **(B)** Nb/U vs. Th/Yb of the Taipa and Coloane leucogranites. PM = primitive mantle normalized. UC = upper crust, MC = middle crust, LC = lower crust of Rudnick and Gao (2003). WUC = upper crust of Wedepohl (1995), WLC = lower crust of Wedepohl (1995). OIB = ocean-island basalt of Sun and McDonough (1989). **(C)** Composition of biotite from the Taipa and Coloane leucogranites expressed as Fe/(Fe+Mg) vs. total (S) Al (apfu) with respected to biotite from within-plate (A-type) granites, continental arc suites, and strongly contaminated and reduced I-type (I-SCR) granites (Shabani et al., 2003). **(D)** $FeO_{total}$-MgO-$Al_2O_3$ discrimination diagram for biotite from anorogenic alkaline suites (A), in peraluminous (including S-type) suites (P), and calc-alkaline orogenic suites (C) from Abdel-Rahman (1994).

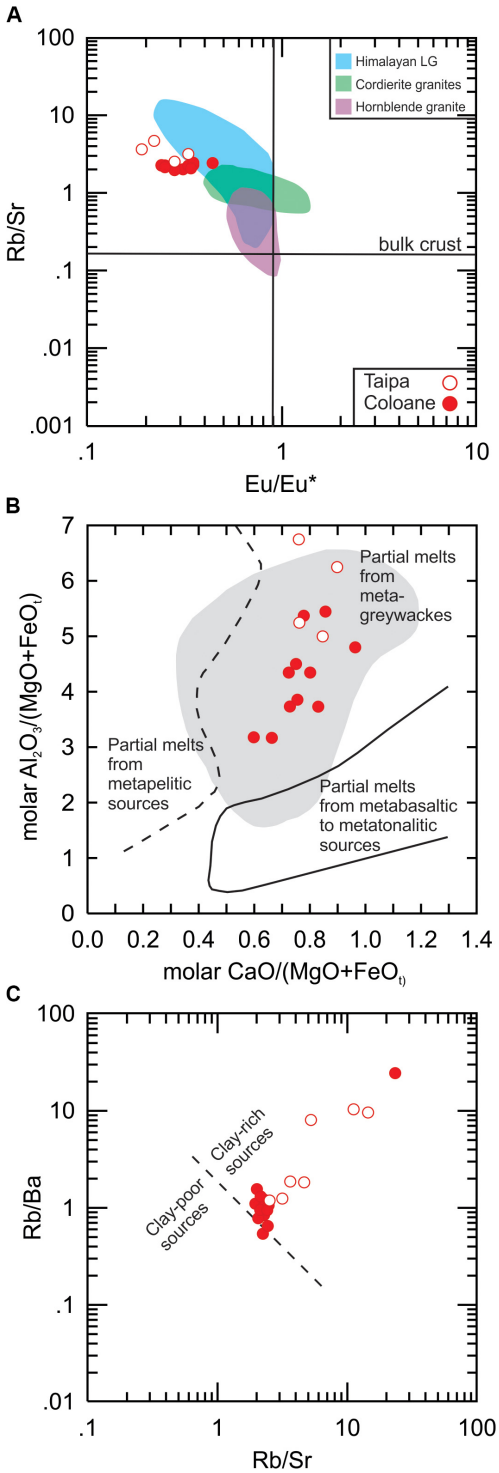


**FIGURE 10 | (A)** Logarithmic Sr/Rb vs. Eu/Eu* plot of the Taipa and Coloane leucogranites with ranges of hornblende granites, Himalayan leucogranites, and cordierite granites from Kemp and Hawkesworth (2003). **(B)** Molar $Al_2O_3$/(MgO + FeOt) vs. molar CaO/(MgO + FeOt) with the fields outlining compositions of melts derived by dehydration melting of different bulk compositions (Altherr et al., 2000). **(C)** Post-collisional strongly peraluminous granites divided into clay-poor and clay-rich sources on the basis of Rb/Ba and Rb/Sr (Sylvester, 1998).

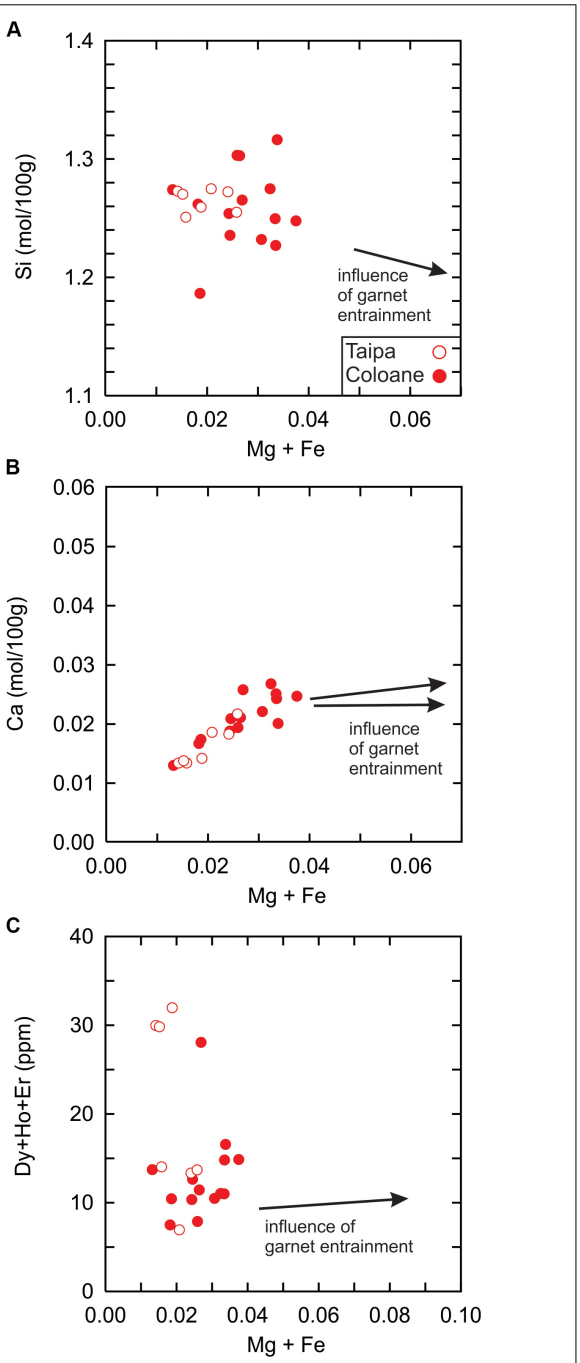


**FIGURE 11 | (A)** Si (molar) vs. maficity (Mg + Fe molar) of the Taipa and Coloane leucogranites. **(B)** Ca (molar) vs. K (molar) of the Taipa and Coloane granites. **(C)** Dy + Ho + Er vs. maficity (Mg + Fe molar) of the Taipa and Coloane leucogranites. The direction of garnet entrainment from Stevens et al. (2007).

melting. The flat chondrite normalized heavy rare earth element patterns ($Gd_N/Yb_N$ = 0.6–1.5) of the rocks is also consistent with the absence of residual garnet in the source (**Figure 5B**). The precise source rock of the leucogranites is uncertain but is likely to be similar to greywacke or metagreywacke. One possible

candidate for the magma source is the Middle Jurassic Tai O Formation, a fine grained sandstone alternating with siltstone and sandy siltstone, in Hong Kong that may be correlative with the Qiaoyuan Formation in Guangdong (Sewell et al., 2000; Wang et al., 2014).

### Implications for the Early Yanshanian Orogeny

The Callovian-Oxfordian stage of the Early Yanshanian Orogeny is markedly different from the Toarcian-Bajocian stage as the nature of the magmatism changes from bimodal to predominately silicic (Li et al., 2007a,b). Moreover, ∼80% or more of the dated Jurassic igneous rocks in the eastern SCB were emplaced during the Callovian-Oxfordian (Li et al., 2007b). The cause of the magmatic flare-up is uncertain but Li and Li (2007); Zhu et al. (2014) suggest that the Callovian-Oxfordian magmatism was related to flat-slab subduction and foundering of the Paleo-Pacific plate followed by mantle up-welling that increased the geotherm and led to volumetrically significant melting of Cathaysia crust. Alternatively, other models suggest that magmatism was related to subduction and slab roll-back of the Paleo-Pacific plate (Jiang et al., 2006, 2009; Wang and Shu, 2012; Zuo et al., 2017).

The leucogranites from Taipa and Coloane based on the distribution of inherited zircons, bulk rock composition, and Sr-Nd-Hf isotopes were primarily derived by partial melting of sedimentary or metasedimentary rocks. The inherited zircons suggest that the source was probably Sinemurian-Pliensbachian in age as it must have accumulated both young and old detritus from the Cathaysia Block. Moreover, the modeling results, temperature and pressure estimates, and bulk rock composition are similar to the genesis of leucogranites that are derived by decompressional melting after the collapse of thickened crust (Sylvester, 1998; Castro et al., 2000; Clemens, 2003; Collins and Richards, 2008). Such a scenario is sufficient to induce melting at lower pressure and is applicable to the rocks of Taipa and Coloane as there is little evidence (e.g., mafic dykes) that indicates a high thermal regime occurred during the Oxfordian (Castro et al., 2000; Li et al., 2004, 2007a,b; Deng et al., 2019).

Whether flat-slab subduction and foundering or subduction and roll-back of the Paleo-Pacific plate was the reason, it is clear there was a major period of magmatism throughout the interior and margin of the eastern SCB from ∼170 Ma to ∼150 Ma and that mafic magmatism was volumetrically minor. The likely scenario for the genesis of the Taipa and Coloane leucogranites is decompression and dehydration melting of the lower upper crust to upper middle crust during a period of extension. The thermal regime associated with the emplacement of the leucogranites is consistent with the limited amount or absence of mafic magmatism during the Callovian-Oxfordian in the region. The location of Taipa and Coloane seems to favor a lithotectonic process that is related to subduction and roll-back as this could not only affect a large area extending from the interior to the margin of Cathaysia but could also induce crustal thinning.

## CONCLUSION

The spessartine-bearing biotite leucogranites from Taipa and Coloane were emplaced during the Late Jurassic (Oxfordian) period of the Yanshanian Orogeny. The biotite chemistry and petrological modeling indicates that the chemical variability within the leucogranites can be attributed to hydrous fractional crystallization at upper to middle crust depth (∼5 to ∼12 km) under reducing conditions (ΔFMQ −1). The Sr-Nd-Hf isotopes [$I_{Sr}$ = 0.71156 to 0.72477; $\varepsilon_{Nd}(t)$ = −7.9 to −8.6; $\varepsilon_{Hf}(t)$ = −3.8 to −8.8], incompatible trace element ratios, and whole rock composition indicates that the leucogranites were derived by partial melting of a sedimentary or metasedimentary source that was comprised of detritus from the Cathaysia Block. Tectonomagmatic discrimination diagrams are consistent with emplacement at a post-collisional tectonic setting. The islands of Taipa and Coloane are very likely the same intrusion and it is possible that they may be members of a larger batholith that extends across the Pearl River estuary to Hong Kong. The formation of the Taipa and Coloane S-type leucogranites is attributed to decompressional melting associated with a period of crustal relaxation or tensional plate stress that may have occurred during the transition from low angle subduction to high angle subduction of the Paleo-Pacific plate.

## DATA AVAILABILITY STATEMENT

All datasets generated for this study are included in the article/ **Supplementary Material**.

## AUTHOR CONTRIBUTIONS

JS conceived the study, collected the samples, and wrote the manuscript. MV assisted in fieldwork and contributed to the ideas expressed. H-YL and YI contributed to the zircon Hf isotope and mineral chemistry measurements. All authors contributed to the manuscript, read, and approved the submitted version.

## FUNDING

This project received support from the Ministry of Science and Technology (Taiwan) through grant 107-2628-M-003-003-MY3.

## ACKNOWLEDGMENTS

PF is thanked for editorial handling. We also appreciate the instrumental influence of Mick, Keith, Charlie, and Ron during field work.

## SUPPLEMENTARY MATERIAL

The Supplementary Material for this article can be found online at: https://www.frontiersin.org/articles/10.3389/feart.2020.00311/full#supplementary-material

## REFERENCES


Abdel-Rahman, A.-F. M. (1994). Nature of biotites from alkaline, calc-alkaline, and peraluminous magmas. *J. Petrol.* 35, 525–541. doi: 10.1093/petrology/35.2.525

Altherr, R., Holl, A., Hegner, E., Langer, C., and Kreuzer, H. (2000). High-potassium, calc-alkaline I-type plutonism in the european variscides: northern Vosges (France) and northern Schwarzwald (Germany). *Lithos* 50, 51–73. doi: 10.1016/s0024-4937(99)00052-3

Andersen, T. (2002). Correction of common lead in U-Pb analyses that do not report 204Pb. *Chem. Geol.* 192, 59–79. doi: 10.1016/s0009-2541(02)00195-x

Andersen, T. (2008). "ComPbCorr-software for common lead correction of U-Th-Pb analyses that do not report 204Pb," in *Laser Ablation-ICP-MS in the Earth Sciences: Current Practices and Outstanding Issues*, ed. P. Sylvester (Quebéc City, QC: Mineralogical Association of Canada), 312–314.

Barbarin, B. (1999). A review of the relationships between granitoids types, their origins and their geodynamic environments. *Lithos* 46, 605–626. doi: 10.1016/s0024-4937(98)00085-1

Blichert-Toft, J., Chauvel, C., and Albarède, F. (1997). The Lu-Hf geochemistry of chondrites and the evolution of the mantle- crust system. *Earth Planet. Sci. Lett.* 148, 243–258. doi: 10.1016/s0012-821x(97)00040-x

Boehnke, P., Watson, E. B., Trail, D., Harrison, T. M., and Schmitt, A. K. (2013). Zircon saturation re-revisited. *Chem. Geol.* 351, 324–334. doi: 10.1016/j.chemgeo.2013.05.028

Castro, A., Corretgé, L. G., El-Biad, M., El-Hmidi, H., Fernández, C., and Patiño Douce, A. E. (2000). Experimental constraints on *Hercynian anataxis* in the Iberian Massif, Spain. *J. Petrol.* 41, 1471–1488. doi: 10.1093/petrology/41.10.1471

Challener, S. C., and Glazner, A. F. (2017). Igneous or metamorphic? hornblende phenocrysts as greenschist facies reaction cells in the half dome granodiorite, California. *Am. Mineral.* 102, 436–444. doi: 10.2138/am-2017-5864

Chappell, B. W., and White, A. J. R. (1974). Two contrasting granite types. *Pacif. Geol.* 8, 173–174.

Chappell, B. W., and White, A. J. R. (2001). Two constrasting granite types: 25 years later. *Aust. J. Earth Sci.* 48, 489–499. doi: 10.1046/j.1440-0952.2001.00882.x

Charvet, J. (2013). The neoproterozoic-early paleozoic tectonic evolution of the South china block: an overview. *J. Asian Earth Sci.* 74, 198–209. doi: 10.1016/j.jseaes.2013.02.015

Chen, J., and Jahn, B.-M. (1998). Crustal evolution of southeastern China: Nd and Sr isotopic evidence. *Tectonophysics* 284, 101–133. doi: 10.1016/s0040-1951(97)00186-8

Chiu, H.-Y., Chung, S.-L., Wu, F.-Y., Liu, D., Liang, Y.-H., Lin, I. J., et al. (2009). Zircon U-Pb and Hf isotopic constraints from eastern transhimalayan batholiths on the precollisional magmatic and tectonic evolution in southern Tibet. *Tectonophysics* 477, 3–19. doi: 10.1016/j.tecto.2009.02.034

Clemens, J. D. (2003). S-type granitic magmas - petrogenetic issues, models and evidence. *Earth Sci. Rev.* 61, 1–18. doi: 10.1016/s0012-8252(02)00107-1

Collins, W. J., and Richards, S. W. (2008). Geodynamic significance of S-type granites in circum-Pacific orogens. *Geology* 36, 559–562.

Corfu, F., Hanchar, J. M., Hoskin, P. W. O., and Kinny, P. (2003). Atlas of zircon textures. *Rev. Mineral. Geochem.* 53, 469–500. doi: 10.2113/0530469

Creaser, R. A., Erdmer, P., Stevens, R. A., and Grant, S. L. (1997). Tectonic affinity of Nisutlin and Anvil assemblage strata from the Teslin tectonic zone, northern Canadian Cordillera: constraints from neodymium isotope and geochemical evidence. *Tectonics* 16, 107–121. doi: 10.1029/96tc03317

Darbyshire, D. P. F., and Sewell, R. J. (1997). Nd and Sr isotope geochemistry of plutonic rocks from Hong Kong: implications for granite petrogenesis, regional structure and crustal evolution. *Chem. Geol.* 143, 81–93. doi: 10.1016/s0009-2541(97)00101-0

Davis, D. W., Sewell, R. J., and Campbell, S. D. G. (1997). U-Pb dating of mesozoic igneous rocks from Hong Kong. *J. Geol. Soc. Lond.* 154, 1067–1076. doi: 10.1144/gsjgs.154.6.1067

Deng, Y., Li, J., Peng, T., Ma, Q., Song, X., Sun, X., et al. (2019). Lithospheric structure in the cathaysia block (South China) and its implication for the Late Mesozoic magmatism. *Phys. Earth Planet. Int.* 291, 24–34. doi: 10.1016/j.pepi.2019.04.003

Dias, A., Quelhas, P., Mata, J., Borges, R., and Lou, V. (2018). *Geologic Map of Macao, Institute of Science and Environment*. Hartford: University of Saint Joseph.

Dong, S., Zhang, Y., Li, H., Shi, W., Xue, H., Li, J., et al. (2018). The yanshan orogeny and the late Mesozoic multi-plate convergence in East Asia - Commemorating 90th years of the "Yanshan Orogeny". *Sci. China Earth Sci.* 61, 1888–1909. doi: 10.1007/s11430-017-9297-y

Dong, Y., and Santosh, M. (2016). Tectonic architecture and multiple orogeny of the qinling orogenic belt, Central China. *Gondwana Res.* 29, 1–40. doi: 10.1016/j.gr.2015.06.009

Freiberg, R., Hecht, L., Cuney, M., and Morteani, G. (2001). Secondary Ca-Al silicates in plutonic rocks and implications for their cooling history. *Contrib. Mineral. Petrol.* 141, 415–429. doi: 10.1007/s004100100241

Frost, B. R., Barnes, C. G., Collins, W. J., Arculus, R. J., Ellis, D. J., and Frost, C. D. (2001). A geochemical classification for granitic rocks. *J. Petrol.* 42, 2033–2048. doi: 10.1093/petrology/42.11.2033

Frost, B. R., Lindsley, D. H., and Andersen, D. J. (1988). Fe-Ti oxide-silicate equilibria: assemblages with fayalitic olivine. *Am. Mineral.* 73, 727–740.

Frost, C. D., and Frost, B. R. (2011). On the ferroan (A-type) granitoids: their compositional variability and modes of origin. *J. Petrol.* 52, 39–53. doi: 10.1093/petrology/egq070

Gao, P., Zheng, Y.-F., and Zhao, Z.-F. (2017). Triassic granites in South China: a geochemical perspective on their characteristics, petrogenesis, and tectonic significance. *Earth Sci. Rev.* 173, 266–294. doi: 10.1016/j.earscirev.2017.07.016

Glazner, A. F., and Johnson, B. R. (2013). Late crystallization of K-feldspar and the paradox of megacrystic granites. *Contrib. Mineral. Petrol.* 166, 777–779.

Griffin, W. L., Pearson, N. J., Belousova, E., Jackson, S. E., van Achterbergh, E., O'Reilly, S. Y., et al. (2000). The Hf isotope composition of cratonic mantle: LAM-MC-ICPMS analysis of zircon megacrysts in kimberlites. *Geochim. Cosmochim. Acta* 64, 133–147. doi: 10.1016/s0016-7037(99)00343-9

Griffin, W. L., Powell, W. J., Pearson, N. J., and O'Reilly, S. Y. (2008). "GLITTER: data reduction software for laser ablation ICP-MS," in *Laser Ablation-ICP-MS in the Earth Sciences: Current Practices and Outstanding Issues*, ed. P. Sylvester (Quebéc City, QC: Mineralogical Association of Canada), 308–311.

Griffin, W. L., Wang, X., Jackson, S. E., Pearson, N. J., O'Reilly, S. Y., Xu, X., et al. (2002). Zircon chemistry and magma mixing, SE China: in-situ analysis of Hf isotopes, Tonglu and Pingtan igneous complexes. *Lithos* 61, 237–269. doi: 10.1016/s0024-4937(02)00082-8

Guitreau, M., Blichert-Toft, J., Martin, H., Mojzsis, S. J., and Albarède, F. (2012). Hafnium isotope evidence from archean granitic rocks for deep-mantle origin of continental crust. *Earth Planet. Sci. Lett.* 337-338, 211–223. doi: 10.1016/j.epsl.2012.05.029

Hammarstrom, J. M., and Zen, E. (1986). Aluminum in hornblende: An empirical igneous geo-barometer. *Am. Mineral.* 71, 1297–1313.

Harrison, T. M., Watson, E. B., and Aikman, A. B. (2007). Temperature spectra of zircon crystallization in plutonic rocks. *Geology* 35, 635–638.

Jackson, S. E., Pearson, N. J., Griffin, W. L., and Belousova, E. A. (2004). The application of laser ablation-inductively coupled plasma-mass spectrometry to in situ U-Pb zircon geochronology. *Chem. Geol.* 211, 47–69. doi: 10.1016/j.chemgeo.2004.06.017

Jahn, B.-M. (2004). "The central Asian orogenic belt and growth of the continental crust in the Phanerozoic," in *Aspects of the Tectonic Evolution of China*, eds J. Malpas, C. J. N. Fletcher, J. R. Ali, and J. C. Aitchison (Bath: Geological Society of London Special Publication), 73–100. doi: 10.1144/gsl.sp.2004.226.01.05

Jiang, Y.-H., Jiang, S.-Y., Dai, B.-Z., Liao, S.-Y., Zhao, K.-D., and Ling, H.-F. (2009). Middle to late Jurassic felsic and mafic magmatism in southern hunan province, southeast China: implications for a continental arc to rifting. *Lithos* 107, 185–204. doi: 10.1016/j.lithos.2008.10.006

Jiang, Y.-H., Jiang, S.-Y., Zhao, K.-D., and Ling, H.-F. (2006). Petrogenesis of Late Jurassic Qianlishan granites and mafic dykes, southeast China: implications for a back-arc extension setting. *Geol. Mag.* 143, 457–474. doi: 10.1017/s0016756805001652

Kemp, A. I. S., and Hawkesworth, C. J. (2003). Granitic perspectives on the generation and secular evolution of the continental crust. *Treatise Geochem.* 3, 349–410. doi: 10.1016/b0-08-043751-6/03027-9

Li, P., Yu, X., Li, H., Qiu, J., and Zhou, X. (2013). Jurassic-cretaceous tectonic evolution of southeast China: geochronological and geochemical constrains of *Yanshanian granitoids*. *Int. Geol. Rev.* 55, 1202–1219. doi: 10.1080/00206814.2013.771952

Li, X.-H., Chung, S.-L., Zhou, H., Lo, C.-H., Liu, Y., and Chen, C.-H. (2004). "Jurassic intraplate magmatism in southern Hunan-eastern Guangxi: 40Ar/39Ar dating, geochemistry, Sr-Nd isotopes and implications for the tectonic evolution of SE China," in *Aspects of the Tectonic Evolution of China*, eds J. Malpas, C. J. N. Fletcher, J. R. Ali, and J. C. Aitchison (Bath: Geological Society of London Special Publication), 193–215. doi: 10.1144/gsl.sp.2004.226.01.11

Li, X.-H., Li, W.-X., and Li, Z.-X. (2007a). On the genetic classification and tectonic implications of the Early Yanshanian granitoids in the Nanling Range, South China. *Chinese Sci. Bull.* 52, 1873–1885. doi: 10.1007/s11434-007-0259-0

Li, X.-H., Li, Z.-X., Li, W.-X., Liu, Y., Yuan, C., Wei, G., et al. (2007b). U-Pb zircon, geochemical and Sr-Nd-Hf isotopic constraints on age and origin of Jurassic I- and A-type granites from central Guangdong, SE China: a major igneous event in response to foundering of a subducted flat slab? *Lithos* 96, 186–204. doi: 10.1016/j.lithos.2006.09.018

Li, X.-H., Li, W.-X., Wang, X.-C., Li, Q.-L., Liu, Y., and Tang, G.-Q. (2009). Role of mantle-derived magma in genesis of early yanshanian granites in the Nanling Range, South China: in situ zircon Hf-O isotopic constraints. *Sci. China Earth Sci.* 52, 1262–1278. doi: 10.1007/s11430-009-0117-9

Li, Z., Qiu, J.-S., and Yang, X.-M. (2014). A review of the geochronology and geochemistry of Late Yanshanian (Cretaceous) plutons along the Fujian coastal area of southeastern China: implications for magma evolution related to slab break-off and rollback in the Cretaceous. *Earth Sci. Rev.* 128, 232–248. doi: 10.1016/j.earscirev.2013.09.007

Li, Z.-X., and Li, X.-H. (2007). Formation of the 1300-km-wide intracontinental orogeny and post-orogenic magmatic province in Mesozoic South China: a flat slab subduction model. *Geology* 35, 179–182.

Li, Z.-X., Li, X.-H., Chung, S.-L., Lo, C.-H., Xu, X., and Li, W.-X. (2012). Magmatic switch-on and switch-off along the South China continental margin since the Permian: transition from an Andean-type to a Western Pacific-type plate boundary. *Tectonophysics* 532–535, 271–290. doi: 10.1016/j.tecto.2012.02.011

Liu, H., Wang, Y., Li, Z., Zi, J.-W., and Huangfu, P. (2018). Geodynamics of the Indosinian orogeny between the South China and Indochina blocks: insights from latest Permian-Triassic granitoids and numerical modeling. *Geol. Soc. Am. Bull.* 130, 1289–1306. doi: 10.1130/b31904.1

Locock, A. J. (2008). An Excel spreadsheet to recast analyses of garnet into end-member components, and a synopsis of the crystal chemistry of natural silicate garnets. *Comput. Geosci.* 34, 1769–1780. doi: 10.1016/j.cageo.2007.12.013

Ludwig, K. R. (1998). On the treatment of concordant uranium-lead ages. *Geochim. Cosmochim. Ac.* 62, 665–676. doi: 10.1016/s0016-7037(98)00059-3

Ludwig, K. R. (2011). Isoplot v. 4.15: a geochronological toolkit for microsoft excel. *Berkel. Geochronol. Center Spec. Public.* 4:70.

Luhr, J. F., Carmichael, I. S. E., and Varekamp, J. C. (1984). The 1982 eruptions of El Chichón volcano, Chiapas, Mexico: mineralogy and petrology of the anhydrite-bearing pumices. *J. Volcanol. Geoth. Res.* 23, 69–108. doi: 10.1016/0377-0273(84)90057-x

Maniar, P. D., and Piccoli, P. M. (1989). Tectonic discrimination of granitoids. *Geol. Soc. Am. Bull.* 101, 635–643. doi: 10.1130/0016-7606(1989)101<0635:tdog>2.3.co;2

Metcalfe, I. (2006). Palaeozoic and mesozoic tectonic evolution and palaeogeography of East Asian crustal fragments: the Korean Peninsula in context. *Gondwana Res.* 9, 24–46. doi: 10.1016/j.gr.2005.04.002

Miller, C. F., McDowell, S. M., and Mapes, R. W. (2003). Hot and cold granites? Implications of zircon saturation temperatures and preservation of inheritance. *Geology* 31, 529–532.

Miller, C. F., and Stoddard, E. F. (1981). The role of manganese in the paragenesis of magmatic garnet: an example from the Old Woman-Piute range, California. *J. Geol.* 89, 233–246. doi: 10.1086/628582

Mutch, E. J. F., Blundy, J. D., Tattitch, B. C., Cooper, F. J., and Brooker, R. A. (2016). An experimental study of amphibole stability in low-pressure granitic magmas and a revised Al-in-hornblende geobarometer. *Contrib. Mineral. Petrol.* 171:85. doi: 10.1007/s00410-016-1298-1299

Nachit, H., Ibhi, A., Abia, E. H., and Ohoud, M. B. (2005). Discrimination between primary magmatic biotites, reequilibrated biotites and neoformed biotites. *C.R. Geosci.* 337, 1415–1420. doi: 10.1016/j.crte.2005.09.002

Nenova, P. I. (1997). Fe23: a computer program for calculating the number of Fe2+ and Fe3+ ions in minerals. *Comput. Geosci.* 23, 215–219. doi: 10.1016/s0098-3004(97)85445-3

Nowell, G. M., Kempton, P. D., Noble, S. R., Fitton, J. G., Saunders, A. D., Mahoney, J. J., et al. (1998). High precision Hf isotope measurements of MORB and OIB by thermal ionization mass spectrometry: insight into the depleted mantle. *Chem. Geol.* 149, 211–233. doi: 10.1016/s0009-2541(98)00036-9

Patiño Douce, A. E. (1999). "What do experiments tell us about the relative contributions of crust and mantle to the origin of granitic magmas?," in *Understanding Granites: Integrating New and Classical Techniques*, eds A. Castro, C. Fernández, and J. L. Vigneresse (Bath: Geological Society of London Special Publication), 55–75. doi: 10.1144/gsl.sp.1999.168.01.05

Pearce, J. A. (1996). Sources and settings of granitic rocks. *Episodes* 19, 120–125. doi: 10.18814/epiiugs/1996/v19i4/005

Pupin, J. P. (1980). Zircon and granite petrology. *Contrib. Mineral. Petrol.* 73, 207–220. doi: 10.1007/bf00381441

Quelhas, P., Dias, A. A., Mata, J., Davis, D. W., and Ribeiro, M. L. (2020). High-precision geochronology of mesozoic magmatism in Macao, southeast China: evidence for multistage granite emplacement. *Geosci. Front.* 11, 243–263. doi: 10.1016/j.gsf.2019.04.011

Ribeiro, M. L., Ramos, J. M. F., Pereira, E., and Dias, R. P. (1992). *Noticia Explicativa da Carta Geologica de Macau na Escala 1/5000*. Lisboa: Servicos Geologicos.

Rossignol, C., Bourquin, S., Hallot, E., Poujol, M., Dabard, M.-P., Martini, R., et al. (2018). The Indosinian orogeny: a perspective from sedimentary archive of north Vietnam. *J. Asian Earth Sci.* 158, 352–380. doi: 10.1016/j.jseaes.2018.03.009

Rudnick, R. L., and Gao, S. (2003). Composition of the continental crust. *Treatise Geochem.* 3, 1–64. doi: 10.1016/b0-08-043751-6/03016-4

Schmidberger, S. S., Heaman, L. M., Simonetti, A., Creaser, R. A., and Whiteford, S. (2007). Lu-Hf, in-situ Sr and Pb isotope and trace element systematics for mantle eclogites from the Diavik diamond mine: evidence for paleoproterozoic subduction beneath the *Slave craton*, Canada. *Earth Planet. Sci. Lett.* 254, 55–68. doi: 10.1016/j.epsl.2006.11.020

Sewell, R. J., and Campbell, S. D. G. (1997). Geochemistry of coeval mesozoic plutonic and volcanic suites in Hong Kong. *J. Geol. Soc. Lond.* 154, 1053–1066. doi: 10.1144/gsjgs.154.6.1053

Sewell, R. J., Campbell, S. D. G., Fletcher, C. J. N., Lai, K. W., and Kirk, P. A. (2000). *The Pre-Quaternary Geology of Hong Kong*. Hong Kong: Geotechincal Engineering Office.

Sewell, R. J., Davis, D. W., and Campbell, S. D. G. (2012). High precision U-Pb zircon ages for mesozoic igneous rocks from Hong Kong. *J. Asian Earth Sci.* 43, 164–175. doi: 10.1016/j.jseaes.2011.09.007

Shabani, A. A. T., Lalonde, A., and Whalen, J. B. (2003). Composition of biotite from granitic rocks of the canadian appalachian orogen: a potential tectonomagmatic indicator. *Can. Mineral.* 41, 1381–1396. doi: 10.2113/gscanmin.41.6.1381

Shellnutt, J. G., Lan, C.-Y., Long, T. V., Ususki, T., Yang, H.-J., Mertzman, S. A., et al. (2013). Formation of cretaceous cordilleran and post-orogenic granites and their microgranular enclaves from the Dalat zone, southern Vietnam: tectonic implications for the evolution of Southeast Asia. *Lithos* 182–183, 229–241. doi: 10.1016/j.lithos.2013.09.016

Shu, L. S., Zhou, X. M., Deng, P., Wang, B., Jiang, S. Y., Yu, J. H., et al. (2009). Mesozoic tectonic evolution of the southeast China block: new insights from basin analysis. *J. Asian Earth Sci.* 34, 376–391. doi: 10.1016/j.jseaes.2008.06.004

Sláma, J., Košler, J., Condon, D. J., Crowley, J. L., Gerdes, A., Hanchar, J. M., et al. (2008). Plešovice zircon - A new natural reference material for U-Pb and Hf isotopic microanalysis. *Chem. Geol.* 249, 1–35. doi: 10.1016/j.chemgeo.2007.11.005

Smith, P. M., and Asimow, P. D. (2005). Adiabat_1ph: a new public front-end to the MELTS, pMELTS, and pHMELTS models. *Geochem. Geophys. Geosyst.* 6:Q02004. doi: 10.1029/2004GC000816

Söderlund, U., Patchett, P. J., Vervoort, J. D., and Isachsen, C. E. (2004). The 176Lu decay constant determined by Lu-Hf and U-Pb isotope systematics of Precambrian mafic intrusions. *Earth Planet. Sci. Lett.* 219, 311–324. doi: 10.1016/s0012-821x(04)00012-3

Stevens, G., Villaros, A., and Moyen, J.-F. (2007). Selective peritectic garnet entertainment as the origin of geochemical diversity in S-type granites. *Geology* 35, 9–12.

Sun, J., Shu, L., Santosh, M., and Wang, L. (2018). Precambrian crustal evolution of the central Jiangnan orogen (South China): evidence from detrital zircon U-Pb

ages and Hf isotopic compositions of neoproterozoic metasedimentary rocks. *Precambrian Res.* 318, 1–24. doi: 10.1016/j.precamres.2018.09.008

Sun, S. S., and McDonough, W. F. (1989). "Chemical and isotopic systematics of oceanic basalts: implications for mantle composition and processes," in *Magmatism in the Ocean Basins*, eds A. D. Saunders and M. J. Norry (Bath: Geological Society of London Special Publication), 313–435.

Sylvester, P. J. (1998). Post-collisional strongly peraluminous granites. *Lithos* 45, 29–44. doi: 10.1016/s0024-4937(98)00024-3

Tanaka, T., Togashi, S., Kamioka, H., Amakawa, H., Kagami, H., Hamamoto, T., et al. (2000). JNdi-1: a neodymium isotopic reference in consistency with LaJolla neodymium. *Chem. Geol.* 168, 279–281. doi: 10.1016/s0009-2541(00)00198-4

Tindle, A. G., and Webb, P. C. (1990). Estimation of lithium contents in trioctahedral micas using microprobe data: application to micas from granitic rocks. *Eur. J. Mineral.* 2, 595–610. doi: 10.1127/ejm/2/5/0595

Uchida, E., Endo, S., and Makino, M. (2007). Relationship between solidification depth of granitic rocks and formation of hydrothermal ore deposits. *Resource Geol.* 57, 47–56. doi: 10.1111/j.1751-3928.2006.00004.x

Unterschutz, J. E., Creaser, R. A., Erdmer, P., Thompson, R. I, and Daughtry, K. L. (2002). North American margin origin of Quesnel terrane strata in the southern Canadian Cordillera: Inferences from geochemical and Nd isotopic characteristics of triassic metasedimentary rocks. *Geol. Soc. Am. Bull.* 114, 462–475. doi: 10.1130/0016-7606(2002)114<0462:namooq>2.0.co;2

Villaros, A., Stevens, G., and Buick, I. S. (2009). Tracking S-type granite from source to emplacement: clues from garnet in the Cape Granite suite. *Lithos* 112, 217–235. doi: 10.1016/j.lithos.2009.02.011

Wang, D., and Shu, L. (2012). Late Mesozoic basin and range tectonics and related magmatism in southeast China. *Geosci. Front.* 3, 109–124. doi: 10.1016/j.gsf.2011.11.007

Wang, Y., Fan, W., Zhang, G., and Zhang, Y. (2013). Phanerozoic tectonics of the South China block: key observations and controversies. *Gondwana Res.* 23, 1273–1305. doi: 10.1016/j.gr.2012.02.019

Wang, Y., Wu, X., Duan, W., and Li, L. (2014). The discovery of Jurassic plants in Shenzhen and Guangdong, southern China and related significance. *Chin. Sci. Bull.* 59, 3630–3637. doi: 10.1007/s11434-014-0449-5

Wang, Y., Zhang, A., Fan, W., Zhao, G., Zhang, G., Zhang, Y., et al. (2011). Kwangsian crustal anataxis within the eastern South China Block: geochemical, zircon U-Pb geochronological and Hf isotopic fingerprints from the gneissoid granites of Wugong and Wuyi-Yunkai domains. *Lithos* 127, 239–260. doi: 10.1016/j.lithos.2011.07.027

Wedepohl, K. H. (1995). The composition of the continental crust. *Geochim. Cosmochim. Acta* 59, 1217–1232.

Whalen, J. B., Currie, K. L., and Chappell, B. W. (1987). A-type granites: geochemical characteristics, discrimination and petrogenesis. *Contrib. Mineral. Petrol.* 95, 407–419. doi: 10.1007/bf00402202

Whitney, D. L., and Evans, B. (2010). Abbreviations for names of rock-forming minerals. *Am. Mineral.* 95, 185–187. doi: 10.2138/am.2010.3371

Wiedenbeck, M., Allé, P., Corfu, F., Griffin, W. L., Meier, M., Oberli, F., et al. (1995). Three natural zircon standards for U-Th-Pb, Lu-Hf, trace element and REE analyses. *Geostandard. Newslett.* 19, 1–23. doi: 10.1111/j.1751-908x.1995.tb00147.x

Wones, D. R., and Eugster, H. P. (1965). Stability of biotite: experiment, theory, and application. *Am. Mineral.* 50, 1228–1272.

Woodhead, J. D., and Hergt, J. M. (2005). A preliminary appraisal of seven natural zircon reference materials for in situ Hf isotope determination. *Geostand. Geoanal. Res.* 29, 183–195. doi: 10.1111/j.1751-908x.2005.tb00891.x

Wu, F.-Y., Yang, Y.-H., Xie, L.-W., Yang, J.-H., and Xu, P. (2006). Hf isotopic compositions of the standard zircons and baddeleyites used in U-Pb geochronology. *Chem. Geol.* 234, 105–126. doi: 10.1016/j.chemgeo.2006.05.003

Wu, G. (2005). The yanshanian orogeny and two kinds of yanshanides in eastern-central China. *Ac. Geol. Sinica* 79, 507–518. doi: 10.1111/j.1755-6724.2005.tb00917.x

Wu, Y.-B., and Zheng, Y.-F. (2013). Tectonic evolution of a composite collision orogeny: an overview on the Qinling-Tongbai-Hong'an-Dabie-Sulu orogenic belt in central China. *Gondwana Res.* 23, 1402–1428. doi: 10.1016/j.gr.2012.09.007

Xu, C., Shi, H., Barnes, C. G., and Zhou, Z. (2016). Tracing a late Mesozoic magmatic arc along the Southeast Asian margin from the granitoids drill from the northern South China Sea. *Int. Geol. Rev.* 58, 71–94. doi: 10.1080/00206814.2015.1056256

Xu, X., O'Reilly, S. Y., Griffin, W. L., Wang, X., Pearson, N. J., and He, Z. (2007). The crust of Cathaysia: age, assembly and reworking of two terranes. *Precambrian Res.* 158, 51–78. doi: 10.1016/j.precamres.2007.04.010

Zeh, A., Gerdes, A., Klemd, R., and Barton, J. M. (2007). Archaean to Proterozoic Crustal evolution in the Central Zone of the Limpopo Belt (South Africa-Botswana): constraints from combined U-Pb and Lu-Hf isotope analyses of zircon. *J. Petrol.* 48, 1605–1639. doi: 10.1093/petrology/egm032

Zhao, G. (2015). Jiangnan Orogen in South China: developing from divergent double subduction. *Gondwana Res.* 27, 1173–1180. doi: 10.1016/j.gr.2014.09.004

Zhou, X., Sun, T., Shen, W., Shu, L., and Niu, Y. (2006). Petrogenesis of mesozoic granitoids and volcanic rocks in south China: a response to tectonic evolution. *Episodes* 29, 26–33. doi: 10.18814/epiiugs/2006/v29i1/004

Zhou, X. M., and Li, W. X. (2000). Origin of Late Mesozoic igneous rocks in southeastern China: implications for lithospheric subduction and underplating of mafic magmas. *Tectonophysics* 326, 269–267.

Zhu, K.-Y., Li, Z.-X., Xu, X.-S., and Wilde, S. A. (2014). A Mesozoic Andean-type orogenic cycle in southeastern China as recorded by granitoid evolution. *Am. J. Sci.* 314, 187–234. doi: 10.2475/01.2014.06

Zindler, A., and Hart, S. (1986). Chemical geodynamics. *Annu. Rev. Earth Planet. Sci.* 14, 493–571.

Zuo, X., Chan, L. S., and Gao, J.-F. (2017). Compression-extension transition of continental crust in a subduction zone: a parametric numerical modeling study with implications on Mesozoic-Cenozoic tectonic evolution of the Cathaysia block. *PLoS One* 12:e0171536. doi: 10.1371/journal.pone.0171536

**Conflict of Interest:** MV was employed by the company Siletzia Resources LLC.

The remaining authors declare that the research was conducted in the absence of any commercial or financial relationships that could be construed as a potential conflict of interest.